



VRIJE  
UNIVERSITEIT  
BRUSSEL



Graduation thesis submitted in partial fulfilment of blah

# SOMETHING ABOUT HIGGS+CHARM

my thesis subtitle

Felix Heyen

March 2026

Promotors: prof. dr. Michael Tytgat    prof. dr. Gerrit Van Onsem

sciences and bioengineering sciences



# Abstract

My abstract



# Contents

<b>Abstract</b>	<b>iii</b>
<b>1 Introduction</b>	<b>1</b>
1.1 The Standard Model of particle physics . . . . .	1
1.2 The Higgs-charm Yukawa coupling . . . . .	3
1.2.1 The Brout-Englert-Higgs mechanism . . . . .	5
1.2.2 The Yukawa couplings . . . . .	7
1.3 Measuring the charm quark Yukawa coupling . . . . .	7
1.3.1 The cH process . . . . .	7
1.3.2 The $\kappa$ -framework . . . . .	8
1.4 An EFT interpretation of the cH process . . . . .	11
1.4.1 The chromomagnetic dipole operator . . . . .	12
1.4.2 Validity of an EFT . . . . .	13
<b>2 The CMS experiment at the LHC</b>	<b>15</b>
2.1 The CMS detector . . . . .	15
2.1.1 The CMS coordinate system . . . . .	15
2.1.2 The silicon tracker . . . . .	17
2.1.3 The electromagnetic calorimeter . . . . .	18
2.1.4 The hadronic calorimeter . . . . .	19
2.1.5 The superconducting solenoid magnet . . . . .	19
2.1.6 The muon chambers . . . . .	20
2.1.7 The triggering system . . . . .	22
2.2 Event reconstruction with the CMS detector . . . . .	22
2.2.1 Track and vertex reconstruction . . . . .	22
2.2.2 The Particle Flow algorithm . . . . .	23
2.2.3 Reconstruction and identification of muons . . . . .	24
2.2.4 Reconstruction and identification of jets . . . . .	25
2.2.5 Missing transverse momentum . . . . .	26
2.3 Identification of charm quark-induced jets . . . . .	27
2.3.1 Properties of heavy-flavour jets . . . . .	27
2.3.2 The DeepJet algorithm . . . . .	28
<b>3 Search for the cH(<math>ZZ \rightarrow 4\mu</math>) process</b>	<b>33</b>
<b>4 An EFT interpretation of the cH(<math>ZZ \rightarrow 4\mu</math>) process</b>	<b>35</b>
<b>Conclusion</b>	<b>37</b>

<b>Bibliography</b>	<b>39</b>
---------------------	-----------

# Chapter 1

## Introduction

The Standard Model (SM) of particle physics is the theory that best describes our current understanding of fundamental particles and their interactions. It describes a broad range of phenomena and makes a plethora predictions for these, many of which have been confirmed via measurement to great degrees of accuracy [1]. A notable feature of the SM is the Brout-Englert-Higgs (BEH) mechanism [2][3], which predicts the existence of a Brout-Englert-Higgs (or often simply Higgs) boson. The EBH mechanism is considered a central part of the SM as it provides a unique mechanism by which SM particles may acquire mass through their interaction with the Higgs boson. As such, the experimental discovery of a Higgs-like scalar boson in 2012 [4][5] was a major milestone in particle physics. Since this discovery, a significant open question in particle physics has been whether this particle indeed behaves entirely in an SM-like way. Measuring the exact properties of the discovered scalar particle has thus been a major feature of LHC experiments such as the CMS collaboration [6]. A significant subset of these properties are the so-called Yukawa interactions between the Higgs boson and massive fermions. As can be seen in Figure 1.1, a number of these have previously been measured and indeed align with the values expected from the SM. However, the measurement of the Yukawa couplings of several of the lighter fermions still remain an open challenge as these couplings decrease in strength with smaller fermion masses.

The next lightest fermion candidate for such a measurement is the charm quark. Consequentially, the study of the Yukawa-coupling between the Higgs boson and the charm quark is of significant interest [7]. Apart from a brief discussion of the SM, this section introduces the charm-Yukawa coupling. Additionally, LHC processes may be targeted to exploit their sensitivity to the Higgs-charm Yukawa coupling with an experiment such as the CMS detector are discussed.

### 1.1 The Standard Model of particle physics

The SM is formulated as through the formalism of Quantum Field Theory (QFT). This is a formalism that combines concepts of classical field theory, quantum mechanics as well as special relativity into a single, coherent description of fundamental particles as excitations of underlying fields that pervade space-time. In this description, SM particles fall into two categories: fermions and bosons. The former are the massive particles which may make up the matter of the universe while the latter are the force-carrying particles of the strong and electro-weak forces. The distinction between these categories is made based on the spin of the particle, which may be of either half-integer or integer respectively.

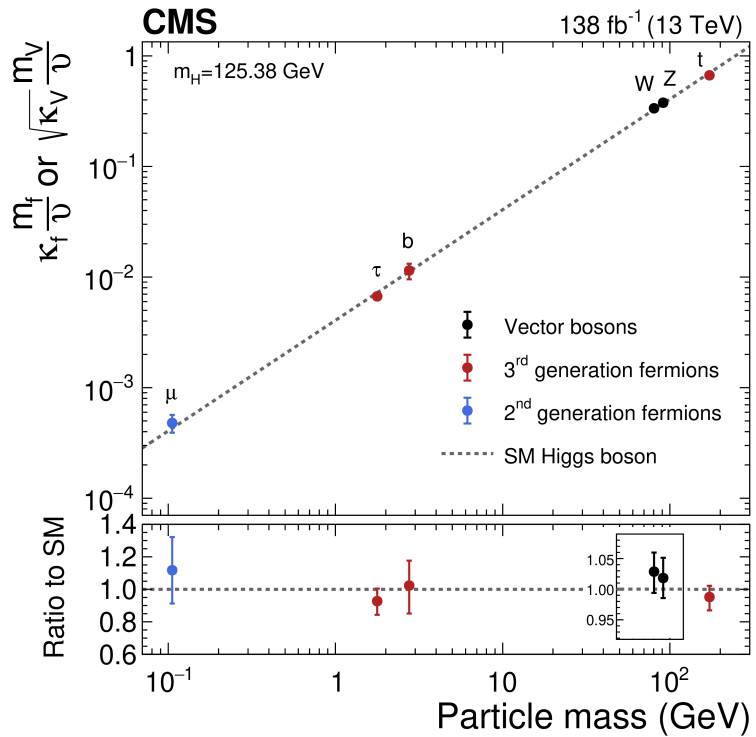


Figure 1.1: The measured coupling modifiers  $\kappa_f$  and  $\kappa_V$  of the coupling between the Higgs boson and fermions as well as heavy gauge bosons as functions of fermion or gauge boson mass  $m_f$  and  $m_V$ , where  $\nu$  is the vacuum expectation value of the Higgs field. [6]

The fermion content of the SM consists of 12 unique particles. These include six leptons, namely the electron, muon and tau as well as their respective neutrinos as well as six different quarks that are distinguished by their so-called flavour. The different quark flavours include up, down, charm, strange, bottom and top and specifies a quark's mass eigenstate as well as electric charge. These fermions are typically arranged into three generations typically depicted as

$$\begin{pmatrix} e \\ \nu_e \end{pmatrix}, \begin{pmatrix} \mu \\ \nu_\mu \end{pmatrix}, \begin{pmatrix} \tau \\ \nu_\tau \end{pmatrix}, \begin{pmatrix} u \\ d \end{pmatrix}, \begin{pmatrix} c \\ s \end{pmatrix}, \begin{pmatrix} t \\ b \end{pmatrix}. \quad (1.1)$$

However, there are distinct differences between the leptons and quarks. Leptons carry integer (or no) charge while quarks carry fractional charges. More importantly, while both quarks and leptons may interact via the electro-weak force, only the quarks interact via the strong force. Due to the nature of the strong force, quarks almost exclusively form composite states called hadrons. Lastly, the existence of anti-fermions must be mentioned. These carry the exact opposite quantum numbers (.e.g charge) as their fermion counterparts, though otherwise behave similarly (take the electron and positron for instance). For simplicity, references to a fermion in this work may be understood as referencing both the fermion and anti-fermion counterpart, unless otherwise explicitly indicated. Examples of the latter are e.g. referring explicitly to electrons  $e^-$  and positrons  $e^+$  or charm quark  $c$  and anti-charm quark  $\bar{c}$  pairs.

There exist 13 unique bosons in the SM. These include the photon  $\gamma$ ,  $W^\pm$  and  $Z$  which mediate the electro-weak force as well as 8 gluons  $g$  that mediate the strong force. The final piece is the Higgs boson. Contrary to the force carriers, which all are spin 1, the Higgs boson is spin 0. By interacting with the Higgs boson, the massive particles of the SM acquire their mass and is thus a central element of the SM.

Considering the introduced particles and forces, the SM has a rich and detailed phenomenology. A great example of a mathematically rigorous delineation of this can be found for example in [8]. Given the focus of this work on the Yukawa coupling between the Higgs boson and charm quark, only this aspect of the SM is discussed in further detail.

## 1.2 The Higgs-charm Yukawa coupling

The coupling that defines the strength of the interaction between massive fermions and the Higgs boson is the so-called Yukawa coupling. To better understand this and associated concepts, some knowledge of the electro-weak sector of the SM is required. These are discussed in this section while a comprehensive overview may be found in [9].

To understand the origin of the Yukawa-couplings, a brief discussion of Lagrangian densities, gauge transformations and the role of symmetries in the SM is warranted. The Lagrangian density  $\mathcal{L}(\phi_i; a_i)$  is a quantity dependent on a set of fields  $\phi_i$  and constants  $a_i$  from which the equations of motions for the particles associated with these fields may be derived. Commonly, theories of particles and their behaviour in a QFT are thus defined through the formulation of a Lagrangian density. The form of this expression determines the nature of the particles that are included as well as their interactions. A central component to the way in which particle interactions are introduced in the SM is the concept of gauge symmetries. These originate from the fact that the quantum fields in a QFT carry phase information, which may depend on the space-time coordinate of the field. This phase information describes (local) degrees of freedom of

the field and should have no effect on the physical observables of the system. Thus,  $\mathcal{L}$  should remain invariant under arbitrary phase transformations. Such transformations are typically referred to as a choice of gauge and such an invariance is accordingly referred to as a *local gauge symmetry*.

In the Lagrangian of the SM, invariance in the presence of local gauge symmetries is insured through the addition of additional fields. These gauge fields couple to the previously existing fields and effectively serve as mediators of phase information between space-time points of the original fields. It is exactly these gauge fields which we identify as the fields force-mediating bosons introduced previously and which are required to maintain local gauge symmetry. A very interesting conclusion from this is that the dynamics of the bosons and the corresponding force are determined entirely by the structure of the local gauge symmetry that must be preserved. For the electro-weak force, the corresponding symmetry is referred to as  $SU(2)_L \times U(1)_Y$ . Here, the  $L$  denotes that the associated force only acts on left-handed chiral particles while the  $Y$  denotes the charge that is carried by the corresponding bosons and is referred to as the weak hypercharge. There are a total of four boson associated with the electro-weak force. These are the photon  $\gamma$  that mediates the electromagnetic force as well as the electromagnetically charged  $W^\pm$  and electromagnetically neutral  $Z$  boson that mediate the weak force.

With these concepts in mind the nature of the electro-weak sector's Lagrangian in the SM may be discussed. Naively, the form of this would be given by

$$\mathcal{L}_{EW} = i\bar{\psi}_L \gamma^\mu D_\mu^L \psi_L + i\bar{\psi}_R \gamma^\mu D_\mu^R \psi_R - \frac{1}{2} \text{Tr} (W_{\mu\nu}^a W^{a\mu\nu}) - \frac{1}{4} B_{\mu\nu} B^{\mu\nu}. \quad (1.2)$$

for a generic combination of a left-handed isospin doublet  $\psi_L$  and right-handed isospin singlet  $\psi_R$ . The individual elements of  $\mathcal{L}_{EW}$  are briefly summarised below

$g'$ :	coupling constant of $U(1)_Y$
$g$ :	coupling constant of $SU(2)_L$
$\psi_L$ ,	left-handed isospin doublet
$\psi_R$ ,	right-handed isospin doublet
$B_\mu$ :	gauge field of $U(1)_Y$
$W_\mu^a$ :	gauge fields of $SU(2)_L$ , $a = 1, 2, 3$
$W_{\mu\nu}$ :	field strength tensor
$B_{\mu\nu}$ :	field strength tensor
$t^a = \frac{\sigma^a}{2}$ ,	$SU(2)$ generators
$Y_L = -1$ ,	left chiral hypercharge
$Y_R = -2$ ,	right chiral hypercharge
$D_\mu^L = \partial_\mu + ig' \frac{Y_L}{2} B_\mu + ig t^a W_\mu^a$	
$D_\mu^R = \partial_\mu + ig' \frac{Y_R}{2} B_\mu$	

The terms  $D_\mu^{L/R}$  are so-called covariant derivatives that ensure the local  $SU(2)_L \times U(1)_Y$  gauge symmetry is upheld for  $\mathcal{L}_{EW}$ . In this formulation, the observed charged gauge bosons  $W^\pm$  arise from linear combinations of the  $W_1$  and  $W_2$  gauge fields

$$W^\pm = \frac{1}{\sqrt{2}}(W_1 \mp iW_2), \quad (1.3)$$

while the Z boson and photon  $\gamma$  arise from linear combinations of the  $W_3$  and  $B$  gauge fields achieved via a rotation

$$\begin{pmatrix} \gamma \\ Z \end{pmatrix} = \begin{pmatrix} \cos\theta_W & \sin\theta_W \\ -\sin\theta_W & \cos\theta_W \end{pmatrix} \begin{pmatrix} B \\ W_3 \end{pmatrix}. \quad (1.4)$$

with the weak mixing angle  $\theta_W$ .

The massive natures of the  $W^\pm$  and Z bosons, as first reported in [10], are however incompatible with such a formulation. This is as naive mass term such as

$$m_W^2 W_\mu^+ W^{-,\mu} + \frac{1}{2} m_Z^2 Z_\mu Z^\mu. \quad (1.5)$$

do not remain invariant under arbitrary  $SU(2)_L$  gauge transformations. This is as gauge fields  $A_\mu$  generically transform as

$$A_\mu \rightarrow A'_\mu = A_\mu - \frac{1}{g} \partial_\mu \mathcal{V}(x) \quad (1.6)$$

where  $\mathcal{V}(x)$  is some arbitrary phase. Substituting Equation 1.6 into Equation 1.5 thus introduces additional terms that do not cancel. The same is true for fermion mass terms in the form of

$$m_f \bar{\psi} \psi. \quad (1.7)$$

There is however a subtle distinction in this case, as the invariance breaking terms in Equation 1.7 arise from the different transformation behaviour of the  $\psi_L$  and  $\psi_R$  components of  $\psi$  under  $SU(2)_L \times U(1)_Y$  gauge transformations.

### 1.2.1 The Brout-Englert-Higgs mechanism

The BEH mechanism provides a way to circumvent the gauge symmetry breaking nature of the aforementioned generic mass terms. This is achieved through a process referred to as spontaneous symmetry breaking. A spontaneously broken symmetry refers to a symmetry that is upheld in a global view of the system (i.e. the overall Lagrangian density  $\mathcal{L}_{EW}$  remains invariant under a relevant gauge transformation) while the energetic ground state of the system explicitly breaks this symmetry. This is a process formally described by the Goldstone theorem [11] that states that each broken symmetry in a relativistic QFT generates an additional massless boson. These introduce additional degrees of freedom into the theory and are coined Goldstone bosons. The

BEH mechanism exploits this by adding an additional term

$$\mathcal{L}_{\text{Higgs}} = D_\mu \phi^\dagger D^\mu \phi - V(\phi) \quad (1.8)$$

$$V(\phi) = -\mu^2 \phi^\dagger \phi + \lambda (\phi^\dagger \phi)^2. \quad (1.9)$$

to  $\mathcal{L}_{\text{EW}}$  with the complex field  $\phi$ . This is a  $SU(2)_L$  doublet

$$\phi = \begin{pmatrix} \phi^+ \\ \phi^0 \end{pmatrix} \quad (1.10)$$

with the scalar components  $\phi^+$  and  $\phi^0$ . Here,  $V(\phi)$  corresponds to the potential energy term of the field. Again, the covariant derivative

$$D_\mu = \partial_\mu + ig' \frac{Y_\phi}{2} B_\mu + igt^a W_\mu^a \quad (1.11)$$

ensures  $\mathcal{L}_{\text{Higgs}}$  remains locally gauge invariant under  $SU(2)_L \times U(1)_Y$  transformations. The constants of the potential term Equation 1.9 are chosen in such a way that the ground state of  $V$  is non-zero. This can be achieved by choosing them such that  $\lambda > 0$  and  $\mu^2 > 0$ . The result is a ground state of  $V$  that is identified as the vacuum expectation

$$v = \sqrt{\frac{\mu^2}{2\lambda}}. \quad (1.12)$$

The center of the potential is now an unstable local maximum and the only stable configuration can be found in the non-zero ground state. Through this, the symmetry of the potential is effectively broken. A popular choice of gauge for  $\phi$  is

$$\phi = \begin{pmatrix} 0 \\ v + \frac{h}{\sqrt{2}} \end{pmatrix} \quad (1.13)$$

where  $h$  is a new scalar field that is used to parametrise radial perturbations of the potential's ground state. This choice is referred to as the unitary gauge and  $h$  is identified as the field corresponding to the physical Higgs boson. By expanding Equation 1.8 with this choice of  $\phi$ , a range of terms are introduced to  $\mathcal{L}_{\text{EW}}$ . These contain a variety of interaction terms between the gauge fields and the Higgs field, as well as newly generated mass terms for the Z and W bosons

$$\left(\frac{g}{2}\right)^2 v^2 W_\mu^+ W^{\mu-} = m_W^2 W_\mu^+ W^{\mu-} \quad (1.14)$$

$$\left(\frac{\sqrt{g^2 + g'}}{2}\right)^2 v^2 Z_\mu Z^\mu = m_Z^2 Z_\mu Z^\mu. \quad (1.15)$$

This can be understood to mean that the electro-weak coupling constants  $g$  and  $g'$  along with  $v$  effectively determine the mass of the Z and  $W^\pm$  bosons. A full description and compilation of all the terms of the electro-weak Lagrangian density of the SM can be found in [9].

### 1.2.2 The Yukawa couplings

By including the Higgs contribution in our theory, mass terms for fermions may now be generated by including a term of the form

$$\mathcal{L}_{\text{Yukawa}} = -y_f \bar{\psi} \phi \psi, \quad (1.16)$$

$$= -y_f v \bar{\psi} \psi \left( 1 + \frac{1}{v} \frac{h}{\sqrt{2}} \right) \quad (1.17)$$

which is invariant under  $SU(2)_L \times U(1)_Y$  gauge transformations due to the addition of  $\phi$ . Similarly to the W and Z mass terms, the relation

$$m_f = y_f v. \quad (1.18)$$

is obtained. A curious feature of the SM is that the Yukawa-couplings  $y_f$  are free parameters of the theory with no a priori values. As a result these must be measured experimentally with the measurement of the charm quark Yukawa coupling  $y_c$  being the goal of this work. As the charm quark mass has previously been determined from experiment to be  $m_c = 1.27$  GeV [1], a measurement of  $y_c$  thus represents an important consistency test of the SM. Another feature that can be read off from Equation 1.17 is that an interaction between fermions and the Higgs field is introduced with an interaction strength proportional to  $y_c$ . It is exactly this feature that may be exploited by experiments at the LHC to measure  $y_c$ .

## 1.3 Measuring the charm quark Yukawa coupling

By measuring the frequency of occurrence of physics processes in which the coupling between the Higgs boson and charm quark appears,  $y_c$  may be determined. As such, a suitable process must be found that can be detected by an experiment such as CMS. These fall into two categories. The first consists of processes in which a Higgs boson decays into a charm and anti-charm quark pair ( $H \rightarrow c\bar{c}$ ). Previous analysis of e.g. top quark pair and vector boson associated Higgs production has been able to observe a 95% CL upper limit on the charm quark Yukawa coupling modifier  $\kappa_c$  (see subsection 1.3.2 for a detailed discussion) of  $\kappa_c < |3.5|$  [12], the most stringent limit to date. The second category consists of processes in which a Higgs boson is produced in association with a charm quark. This latter category of processes is the focus of this work and is henceforth referred to as the cH process.

### 1.3.1 The cH process

The cH process encompasses processes in proton-proton collisions in which a charm-quark is produced alongside a Higgs boson. At leading order, this consists of 2 processes sensitive to  $y_c$ , represented by the Feynman diagrams shown in Figure 1.3. The first two diagrams, namely the s and t-channel diagrams, constitute the  $y_c$  sensitive contribution. There exist also additional processes cH, mediated through the effective Higgs boson to gluon coupling, which are not sensitive to  $y_c$ . These account for approximately 80% of the inclusive cH cross section and thus represents a significant background to the cH process sensitive to the charm quark Yukawa coupling.

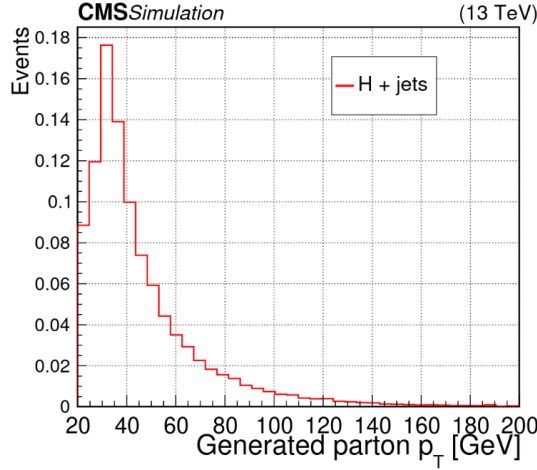


Figure 1.2: Transverse momentum of the charm quark produced alongside a Higgs boson in a simulation of the cH process, which typically takes on relatively small values. THIS IS A PLACEHOLDER PLOT.

Targeting the cH process to measure  $y_c$  is a relatively novel strategy in comparison to analyses that target  $H \rightarrow c\bar{c}$ . A key advantage of this approach is that contributions from the abundant QCD background at the LHC are greatly reduced due to only needing to identify the flavour of single jet resulting from a charm quark, as opposed to two. Additionally, since the sensitivity to  $y_c$  does not originate from the decay of the Higgs boson, the Higgs boson decay mode to target can be chosen freely. Especially signatures such as  $H \rightarrow ZZ \rightarrow 4\mu$ , which may be resolved cleanly by an experiment such as CMS, can be targeted. However, targeting the cH process also comes with drawbacks. A significant experimental difficulty results from the fact that the associated charm flavour jet are typically produced at very low transverse momenta  $p_T$ , as seen in Figure 1.2. These can be experimentally difficult to reconstruct and thus a significant portion of this signal may be lost due to detector acceptance effects. Another drawback is that Higgs boson decay channels such as  $H \rightarrow ZZ \rightarrow 4\mu$  have very small branching ratios (e.g.  $\text{BR}(H \rightarrow ZZ \rightarrow 4\mu) = 0.3\%$  [1]) and thus the overall cross section of the cH process may be very small. As a result of these effects, a key challenge of a search for the cH process is expected to lie in its statistical uncertainty.

The cH process is of recent interest and results in the cH(WW) and cH( $\gamma\gamma$ ) channels using Run 2 data of the CMS experiment are published. Upper limits on  $\kappa_c$  at 95% CL are reported with  $|\kappa_c^{\text{cH(WW)}}| < 47$  [13] and  $|\kappa_c^{\text{cH}(\gamma\gamma)}| < 38.1$  [14]. While not as sensitive as the limit observed in the  $H \rightarrow c\bar{c}$  channels, these nonetheless provide important complementary results and can contribute significantly in combination. This is especially important given that even at the High-Luminosity LHC, the projected sensitivity on the charm quark Yukawa coupling in individual channels is only starting to approach one [15].

### 1.3.2 The $\kappa$ -framework

The  $\kappa$ -framework [16] is a tool to parametrise modifications to couplings between the Higgs boson and other particles with respect to the expected SM values of the couplings. For example, the coupling modifiers for the charm quark Yukawa coupling is introduced as

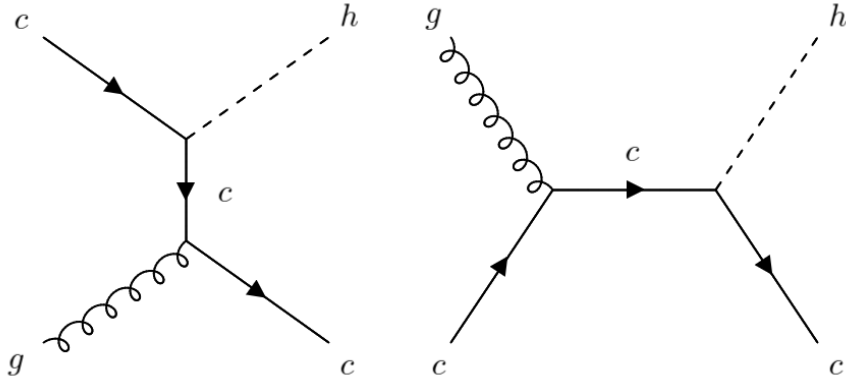


Figure 1.3: The leading order  $cH$  processes through which  $y_c$  may be probed, as each diagramm contains a vertex with a charm-quark and Higgs boson. The corresponding diagrams with an anti-charm quark  $\bar{c}$  are implied.

$$\kappa_f = \frac{y_f}{y_f^{\text{SM}}}. \quad (1.19)$$

where  $y_f$  is the measured Yukawa-coupling and  $y_f^{\text{SM}}$  is the expected Yukawa-coupling of the SM, calculated from the known charm quark mass. Thus modifications to the Yukawa-coupling of the charm quark are parametrised in this way as deviations from  $\kappa_c = 1$ . However,  $y_c$  is not a quantity that can be measured directly. Instead a signal strength measurement  $\mu_{if}$ , where  $i$  represents the production process and  $f$  represents the decay process, relative to the SM expectation is made. Thus a measurement of  $\mu_{if}$  must be converted into an interpretation of  $\kappa_c$ . This is a step that contains some finer subtleties.

The rate of a Higgs production and decay process in relation to the expected SM signal (i.e. a signal strength) may be written as

$$\mu_{if} = \frac{\sigma_i \cdot \text{BR}_f}{(\sigma_i \cdot \text{BR}_f)^{\text{SM}}}, \quad (1.20)$$

where  $\sigma_i$  is the production cross section in a given channel  $i$  and  $\text{BR}_f$  is the decay branching ratio in a given channel  $f$ . This can be rewritten as

$$\sigma_i \cdot \text{BR}_f = \kappa_{r,i} \sigma_i^{\text{SM}} \cdot \frac{\kappa_f \Gamma_f^{\text{SM}}}{\Gamma_H} \quad (1.21)$$

to give a general expression in which modifications to the production cross section and partial SM decay width  $\Gamma_f^{\text{SF}}$  are introduced via  $\kappa_{r,i}$  and  $\kappa_f$  respectively. The denominator  $\Gamma_H$  represents the total decay width which can be written as

$$\begin{aligned} \Gamma_H &= \Gamma_H^{\text{SM}} (\kappa_b^2 \text{BR}_{bb}^{\text{SM}} + \kappa_W^2 \text{BR}_{WW}^{\text{SM}} + \kappa_g^2 \text{BR}_{gg}^{\text{SM}} + \kappa_\tau^2 \text{BR}_{\tau\tau}^{\text{SM}} + \kappa_Z^2 \text{BR}_{ZZ}^{\text{SM}} + \kappa_c^2 \text{BR}_{cc}^{\text{SM}} \\ &\quad + \kappa_\gamma^2 \text{BR}_{\gamma\gamma}^{\text{SM}} + \kappa_{Z\gamma}^2 \text{BR}_{Z\gamma}^{\text{SM}} + \kappa_s^2 \text{BR}_{ss}^{\text{SM}} + \kappa_\mu^2 \text{BR}_{\mu\mu}^{\text{SM}}) \end{aligned} \quad (1.22)$$

$$:= \Gamma_H^{\text{SM}} \kappa_H^2 \quad (1.23)$$

Here,  $\Gamma_H^{\text{SM}}$  is the SM total decay width of the Higgs boson and  $\text{BR}_f^{\text{SM}}$  are the branching ratios of the possible decay modes (the loop induced coupling of the Higgs boson to gluons and photons are included as independent quantities) where  $\kappa_f$  parametrises modifications thereof. Substituting Equation 1.23 into Equation 1.20, the rate modifier may be written as

$$\mu_{if} = \frac{\kappa_{r,i}^2 \kappa_f^2}{\kappa_H^2}. \quad (1.24)$$

Now, assuming in the production of the Higgs boson only modifications to the charm quark Yukawa coupling plays a role as well as that the decay mode (e.g.  $H \rightarrow ZZ \rightarrow 4\mu$ ) is unmodified, Equation 1.24 becomes

$$\mu_{if} = \frac{\kappa_c^2}{\kappa_H^2}. \quad (1.25)$$

Using the flat direction approach discussed in [7] and [17], a simplification of  $\kappa_H$  can be introduced. This approach is based on the finding that, when performing fits to existing Higgs boson production and decay rates, increases in the Yukawa couplings of light quarks (including the charm quark) can be compensated by increases in the couplings of the gauge bosons and heavy fermions. This is referred to as a “flat direction” in the fit, where observed Higgs boson production and decay rates can be modeled equally well for any value of  $\kappa_c$  by a respective scaling of all other processes. The authors thus replace the individual modifiers in the sum of Equation 1.22 with a single modifier  $\kappa$ . This allows Equation 1.24 to be rewritten as

$$\mu_{if} = \frac{\kappa^4}{\kappa^2(1 - \text{BR}_{cc}^{\text{SM}}) + \kappa_c^2 \text{BR}_{cc}^{\text{SM}}} \quad (1.26)$$

which has a solution for  $\kappa$  given by

$$\kappa = \frac{(1 - \text{BR}_{cc}^{\text{SM}})\mu}{2} + \frac{\sqrt{(1 - \text{BR}_{cc}^{\text{SM}})^2\mu^2 + 4\mu\text{BR}_{cc}^{\text{SM}}\kappa_c^2}}{2}. \quad (1.27)$$

Here, the expected SM decay width  $\text{BR}_{cc}^{\text{SM}} = 0.3$  can be substituted. Additionally, the fact that observed Higgs boson rates have been well measured to be close to their expected values (see e.g. [18]) can be reflected by setting  $\mu \approx 1$ , so that only a dependence on  $\kappa_c$  remains in the expression. Thus by replacing  $\kappa_H$  in Equation 1.25 with Equation 1.27, a final expression relating a measured signal strength of the  $cH$  process to  $\kappa_c$  is obtained, given by

$$\mu_{\sigma_{cH}\text{BR}(H \rightarrow ZZ)} = \frac{2\kappa_c^2}{0.97 + \sqrt{(0.97)^2 + 4 \cdot 0.97\kappa_c^2}}. \quad (1.28)$$

Rearranging for  $\kappa_c$  gives

$$\kappa_c = \pm \frac{\sqrt{4 \cdot 0.97 \cdot \mu_{\sigma_{cH}\text{BR}(H \rightarrow ZZ)} \cdot (1 + \mu_{\sigma_{cH}\text{BR}(H \rightarrow ZZ)})}}{2}. \quad (1.29)$$

Effectively, this approach in interpreting  $\kappa_c$  from a signal strength measurement  $\mu_{\sigma_{cH}\text{BR}(H \rightarrow ZZ)}$  thus ensures compatibility with existing Higgs boson rate measurements, given a non-unity value of  $\kappa_c$  leads to modifications of the Higgs boson partial decay widths. It should be noted that this already indirectly implies bounds on  $\kappa_c$ , as discussed in [7].

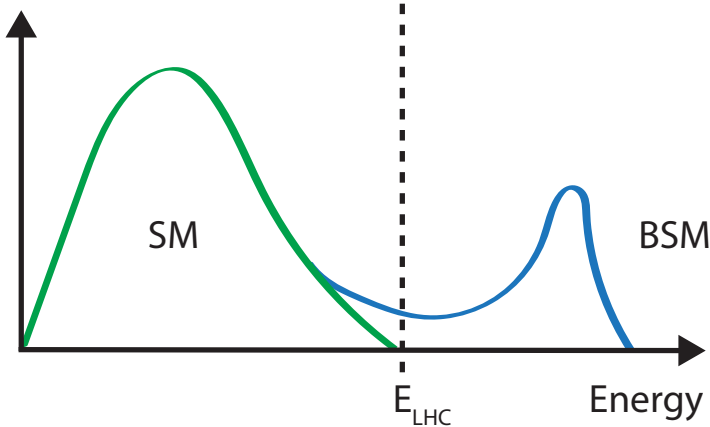


Figure 1.4: Illustration of how the presence of BSM physics, which is primarily visible beyond the reach of current collider energies (e.g.  $E_{\text{LHC}}$ ), can lead to subtle modifications of SM observables. These effects can be parametrised by SMEFT.

## 1.4 An EFT interpretation of the cH process

The cH process may also be interpreted in terms of Standard Model Effective Field Theory (SMEFT). In SMEFT theory, potential effects from physics processes not described by the SM (commonly referred to as beyond-the-SM or BSM physics) are parametrised in a mostly model-independent way. Specifically, the SMEFT framework can be used at colliders with a characteristic energy scale  $E$  to describe the effects of processes with a characteristic energy scale above  $E$ . This concept is illustrated in Figure 1.4.

Formally, SMEFT is a collection of all allowed interaction terms between fields that obey the rules of the SM. Most importantly, this means that said terms satisfy the gauge invariance conditions of the SM. Generically, this can be expressed as an expansion in the energy scale of the new physics scale  $\Lambda$

$$\mathcal{L}_{\text{SMEFT}} = \mathcal{L}_{\text{SM}} + \sum_{d>4} \sum_i \frac{C_i}{\Lambda^{d-4}} \hat{O}_i^d \quad (1.30)$$

where  $\mathcal{L}_{\text{SM}}$  is the SM lagrangian,  $O_i$  denotes a particular operator with a dimensionless coupling coefficient  $C_i$  and  $d$  denotes the dimension of the operator. This latter property arises from a dimensional analysis of a lagrangian and its fields, where energy dimensions of terms may be deduced from the requirement that the action

$$S = \int \mathcal{L} d^4x \quad (1.31)$$

remains dimensionless. As a result,  $\mathcal{L}_{\text{SM}}$  is of energy dimension four. Since  $\Lambda$  carries an energy

dimension of one, terms in the sum of Equation 1.30 scaled with  $1/\Lambda^{d-4}$  must be compensated with an appropriate dimension of the operator  $O_i^d$  to ensure the overall terms also remain of energy dimension four. Consequently, operators in SMEFT are grouped by their energy dimension. In  $d=5$ , only one operator possible operator exists that violates lepton number [19] and is not relevant in this work. In  $d=6$  however, a plethora of valid operators exist. In total, these amount to 59 different dimension six operators (modulo all possible flavour combinations), commonly represented in the Warsaw basis [20]. Since  $d=7$  operators again violate lepton number and each additional dimension adds a suppressive factor of  $\Lambda^{-1}$ , a simplified SMEFT schema is commonly used in which only the contribution of  $d=6$  operators is considered in the expansion. Thus Equation 1.30 simplifies to

$$\mathcal{L}_{\text{SMEFT}} = \mathcal{L}_{\text{SM}} + \sum_i \frac{C_i}{\Lambda^2} \hat{O}_i^{(6)} \quad (1.32)$$

A good overview of SMEFT can be found in [21].

### 1.4.1 The chromomagnetic dipole operator

A particular operator relevant to this work is referred to as the chromomagnetic dipole (CMD) operator  $\hat{O}_{qG}$ . For the charm quark, the CMD operator is written as

$$\hat{O}_{cG} = (\bar{q}_{2,L} \sigma^{\mu\nu} T^a c) \tilde{\phi} G_{\mu\nu}^a. \quad (1.33)$$

Here,  $\bar{q}_{2,L}$  is the second generation, left-handed quark doublet,  $\sigma^{\mu\nu} = i[\gamma_\mu, \gamma_\nu]/2$  with the Dirac matrices  $\gamma_\mu$ ,  $T^a c$  are the generators of the SU(3),  $\tilde{\phi}$  is the adjoint Higgs doublet and  $G_{\mu\nu}^a$  is the field strength tensor of the strong interaction. This operator  $\hat{O}_{cG}$  may be uniquely bounded with the cH process. This is due to two main factors, including the unique chiral structure of the operator, which mixes left and right-handed spinors, otherwise only found in the Yukawa and quark-Higgs boson interaction terms of the SM.

To better understand this, it is worth considering other processes such as inclusive Higgs boson production, which have been successfully leveraged to set strong constraints on the top quark CMD operator  $\hat{O}_{tG}$  [askNordin]. Typically, the strategy that is used to probe even small wilson coefficients e.g.  $C_{tG}$  is to exploit interference of the relevant (small) SMEFT contribution with a larger SM contribution. Though the pure SMEFT contribution itself may be small and experimentally neglible due to limited analysis sensitivity, the much larger contribution of the SM process it interferes with can result in a non-negligeble interference effect with respect to the SM process. However, the chiral structure of the CMD operator influences the effectiveness of this strategy. Since the  $\hat{O}_{qG}$  operator effectively flips the chirality of the ingoing and outgoing quarks, a second *chirality flip* must be inserted for the SMEFT contribution to interfere with the SM process. This is visualised in Figure 1.5. Such a chirality flip is proportional to the mass  $m_q$  of the respective quark. As a result the interference contribution for a much lighter quark is significantly supressed, as also argued for the bottom quark in [22]. Effectively, the processes that prove effective in targeting  $\hat{O}_{tG}$  due to the large mass of the top quark are much less sensitive to  $\hat{O}_{cG}$ . Due to the cH process itself containing the chirality flipping quark-Higgs boson vertex, interference terms between the EFT and SM contributions do not suffer from such

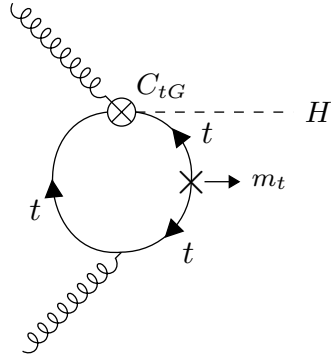
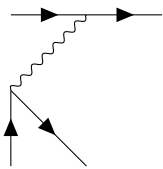


Figure 1.5: A modification of the gluon fusion process with a top quark loop by including the vertex introduced by the top quark CMD operator. Note that the arrows indicate chirality and not momentum flow. A chirality flip, denoted by the cross, proportional to the top quark mass  $m_t$  is required for the inclusion of the top quark CMD vertex.



an effect. Furthermore, due to the very low expected cross section of the cH process, quadratic contributions from  $\hat{O}_{cG}$  may be comparatively large even at small values of  $C_c G$ . As a result, the cH process may be an excellent target in constraining  $\hat{O}_{cG}$ .

#### 1.4.2 Validity of an EFT

In addition to EFT terms needing to satisfy the gauge invariance conditions of the SM, two additional key validity conditions are typically required of an EFT. The first is related to the fact that in an EFT, the particle nature of e.g. new, heavy mediator particles is simplified into the introduction of a new effective vertex. For example, a  $2 \rightarrow 2$  particle resonant scattering via a new heavy mediator particle  $\Omega$  with a newly introduced coupling constant  $g_*$  is simplified via the introduction of a four-point interaction, as visualised in ???. This corresponds to a a first order approximation of the new particle's mediator as

$$\frac{g_*}{p^2 - m_\Omega} \xrightarrow{m_\Omega^2 \gg p^2} -\frac{g_*}{m_\Omega} \left( 1 + \frac{p^2}{m_\Omega^2} + \frac{p^4}{m_\Omega^4} + \dots \right) \approx -\frac{g_*}{m_\Omega} \quad (1.34)$$

For the EFT description of this simplification to be valid, the energy involved in processes containing the effective vertex introduced by the relevant operator must thus lie well below  $m_\Omega$ , which represents the previously introduced new physics scale  $\Lambda$ . Practically, this can be achieved by placing an upper limit  $M_{\text{cut}}$  on the total energy that is considered in measurements of such processes. The requirement can be expressed as

$$M_{\text{cut}} < \Lambda. \quad (1.35)$$

A good estimator of  $M_{\text{cut}}$  is the invariant mass of the final state particles of a process. In case

of the cH process, the invariant mass of the Higgs boson and jet system is a natural choice.

The second condition that must be met is related to the perturbativity of the theory. Concretely, this means that higher dimensional operators should contribute increasingly smaller corrections so that the sum of operator contributions converges. In the case of this work where only d=6 operators are considered, this means ensuring contributions from d=8 operators are sufficiently small. While this cannot be determined with certainty without explicit knowledge of the underlying theory the EFT is estimating, a popular choice is to require that at most  $g_* \sim 4\pi$  [23].

These two conditions may be combined into a single, simultaneous requirement. In [23] an effective lagrangian (ignoring relevant indices for simplicity) of the general form

$$\mathcal{L}_{\text{eff}} = \frac{\Lambda^4}{g_*^2} \mathcal{L} \left( \frac{D_\mu}{\Lambda}, \frac{g_h \phi}{\Lambda}, \frac{g_{\psi_{L,R}} \psi_{L,R}}{\Lambda^{3/2}}, \frac{g F_{\mu\nu}}{\Lambda^2} \right) \quad (1.36)$$

is obtained when a single BSM coupling  $g_*$  is introduced. This provides a prescription for the powers of the couplings and  $\Lambda$  that are associated with the SM fields  $\phi, \psi$  and  $F_{\mu\nu}$ , and the covariant derivative  $D_\mu$ . Here,  $g$  represents the unaltered gauge field couplings of the SM, while  $g_{\psi_{L,R}}$  and  $g_h$  represent the coupling of SM fermion and the Higgs doublet to the BSM theory. In a single BSM coupling scenario, this simplifies to  $g_{\psi_{L,R}} = g_h = g_*$ . Applying this prescription to the CMD operator gives

$$\hat{O}_{cG} \rightarrow \frac{\Lambda^4}{g_*^2} \left[ \left( \frac{g_* \psi_{L,R}}{\Lambda^{3/2}} \right) \cdot \left( \frac{g_* \psi_{L,R}}{\Lambda^{3/2}} \right) \cdot \left( \frac{g_* \phi}{\Lambda} \right) \cdot \left( \frac{g_s G}{\Lambda^2} \right) \right] \quad (1.37)$$

$$= \frac{g_* g_s}{\Lambda^2} (\psi_{L,R} \cdot \psi_{L,R} \cdot \phi \cdot G) . \quad (1.38)$$

Reading off from Equation 1.38, one can see that the coupling of the CMD operator is given by  $g_* g_s / \Lambda^2$ . Comparing to Equation 1.30 thus reveals that the CMD Wilson coefficient is given by  $C_{cG} = g_* g_s$ . By requiring the first validity condition, the relation

$$\frac{C_{cG}}{\Lambda^2} < \frac{g_* g_s}{M_{\text{cut}}^2} \quad (1.39)$$

is obtained. Since both  $C_{cG}$  and  $\Lambda$  are a priori unknown, we can redefine  $\tilde{C}_{cG} = \frac{C_{cG}}{\Lambda^2}$ . With this redefinition and by setting  $g_* \sim 4\pi$ , the expression

$$\frac{|\tilde{C}_{cG}| M_{\text{cut}}^2}{4\pi g_s} < 1 . \quad (1.40)$$

can be used to define a plane in  $\tilde{C}_{cG}$  and  $M_{\text{cut}}$  that satisfies the previously discussed conditions.

## Chapter 2

# The CMS experiment at the LHC

The Compact Muon Solenoid (CMS) detector [24] is large, general purpose particle detector located at the Large Hadron Collider (LHC)[25] accelerator in Geneva, Switzerland. Run by the European Organisation for Nuclear Research (CERN), the LHC’s largest ring spans a circumference of 27km, making it the largest particle accelerator in the world. In their circular trajectory through the beam pipe, collimated bunches of  $\sim 10^{11}$  protons are accelerated in both directions of the ring. At each of the four collision points, of which CMS is built around one, the trajectories of these proton bunches are crossed such that highly energetic proton-proton collisions are produced. A sketch of the LHC accelerator complex can be seen in Figure 2.1. A detector such as CMS effectively acts as a camera taking very complex snapshot of each collision. During Run 2 of the LHC, approximately 30 protons collide on average per bunch crossing with a centre of mass energy of  $\sqrt{s} = 13$  TeV. These collisions produce a plethora of particles, many of which decay to particles of varying multiplicities themselves. As such, these collisions produce a complex and varied phenomenology that require a complex machine such as the CMS detector to fully capture. By capturing the information from many millions of collisions, a multitude of different statistical analyses may be performed on the captured data. This includes analyses of the Higgs boson and its properties, such as the Yukawa coupling of the charm quark. To this end, this chapter gives an overview of the CMS detector and its subsystems as well as the techniques used to reconstruct individual proton-proton collisions.

## 2.1 The CMS detector

The CMS detector is designed to be able to detect a wide range of signatures and is built from a set of complementary sub-detectors. An overview of the detector may be seen in Figure 2.2. By combining data from these sub-detectors, a comprehensive reconstruction of individual proton-proton collisions, commonly referred to as an *event*, may be made. The role and functioning of the individual sub-detectors is covered in this section. While several of the detector components have undergone changes for the current Run-3 of the LHC[28], the configuration relevant to this work is that of Run-2.

### 2.1.1 The CMS coordinate system

Due to the cylindrical nature of the CMS detector, using cylindrical coordinates to describe positions within the detector is a natural choice. Thus, the  $z$  coordinate describes the position along the beam pipe,  $r$  the radius and  $\phi$  the azimuthal angle, where the proton-proton collision

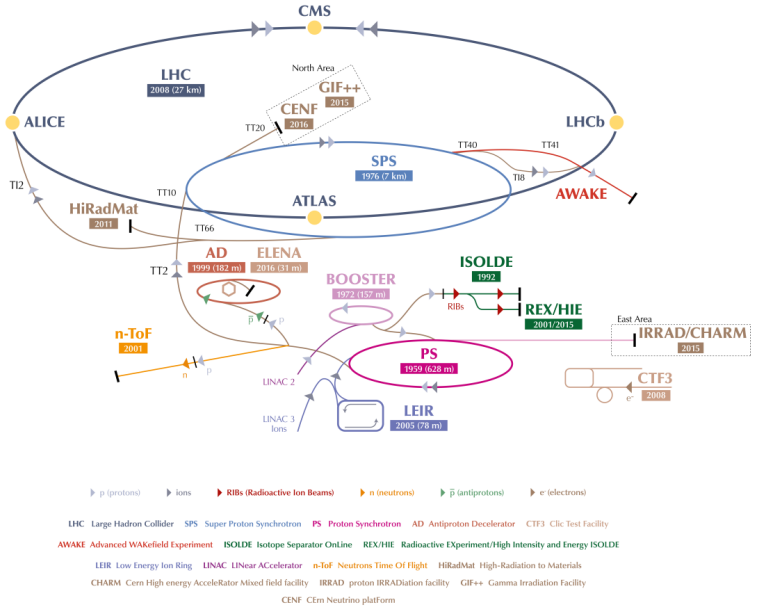


Figure 2.1: An overview of the LHC accelerator complex [26]. Before entering the large LHC ring, particles must pass through a number of increasingly powerful set of accelerators.

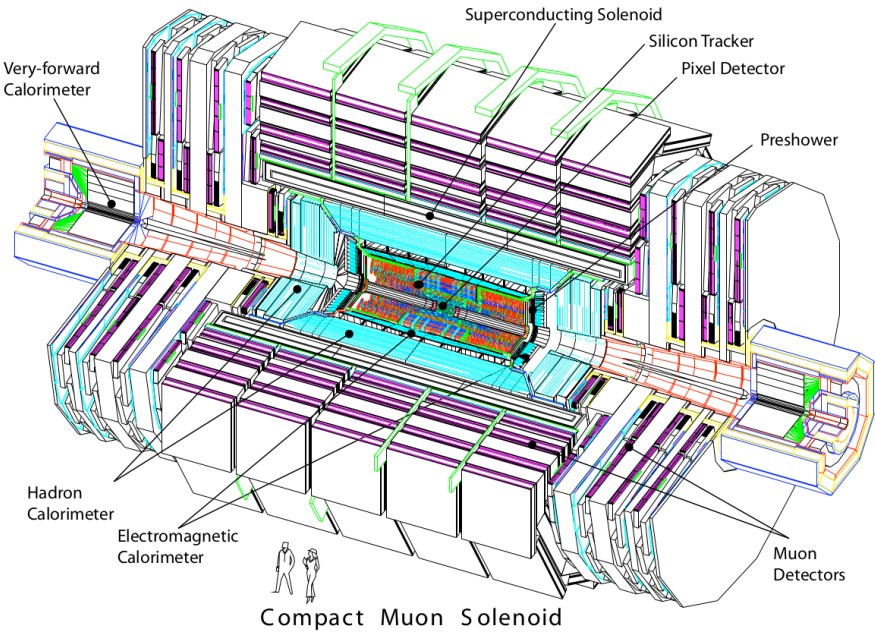


Figure 2.2: An overview of the CMS detector [27].

point is taken as the coordinate system's centre. Trajectories of particles with energy  $E$  within the detector into the plane perpendicular to  $z$  may be described by the rapidity

$$y = \ln \sqrt{\frac{E + p_z c}{E - p_z c}}. \quad (2.1)$$

Small momenta in the  $z$ -direction  $p_z$  give a rapidity of zero, while the rapidity tends to  $\pm\infty$  for large  $p_z$ . However, this requires knowledge of  $E$  and  $p_z$ , which can be difficult to measure. By assuming the particle is ultra-relativistic, as is typically the case at the LHC, it is possible to simplify this description and introduce the pseudorapidity

$$\eta = \ln \left( \tan \left( \frac{\theta}{2} \right) \right) \quad (2.2)$$

which is dependent solely on  $\theta$ , the polar angle. A convenient feature of the (pseudo)rapidity is that differences of (pseudo)rapidity are Lorentz invariant and thus not dependant on the initial longitudinal boost of the proton-proton system, which is a priori not known due to the varying momenta fractions of its constituents. Together with the particle's transverse (to the beam axis) momentum  $p_T$  and mass  $m$ , a particle's four-vector may be defined as

$$p = \begin{pmatrix} m \\ p_T \\ \eta \\ \phi \end{pmatrix}. \quad (2.3)$$

The CMS detector may be broadly split into two distinct regions inward and outward of the boundary  $|\eta| = 1.479$ . The inner region or *barrel* consists of concentric layers around the beam pipe. The outer *endcap* region consists of two caps that close off the detector at either end. In this way, the CMS detector is designed for the best possible hermetic coverage around the collision point.

### 2.1.2 The silicon tracker

The silicon tracker [29] is the innermost system of the CMS detector, situated closest to the beampipe. It is designed to track the trajectories of charged particles as they emerge from the collision point with minimal energy losses to the particles themselves. This subdetector is split into two main components, the pixel detector and silicon strip detector. A sketch of these components may be seen in Figure 2.4.

The pixel detector is situated right around the beampipe and as of 2017 consists of four circular layers of individual silicon pixels in the barrel region and three disk layers in the endcap region. These consist of rectangular silicon chips with a size of  $100 \times 150 \mu\text{m}^2$ . When a charged particle traverses through the active material of these chips, an electrical signal is induced that is recorded. This is typically referred to as a *hit*. The small pixel size allows for position measurements with very high resolution, namely  $\sim 10 \mu\text{m}$  in the  $r\phi$  direction and  $\sim 20 \mu\text{m}$  in the  $z$  direction [30]. An important feature of the pixel detector is its high radiation tolerance due to the close proximity of these modules to the beam pipe.

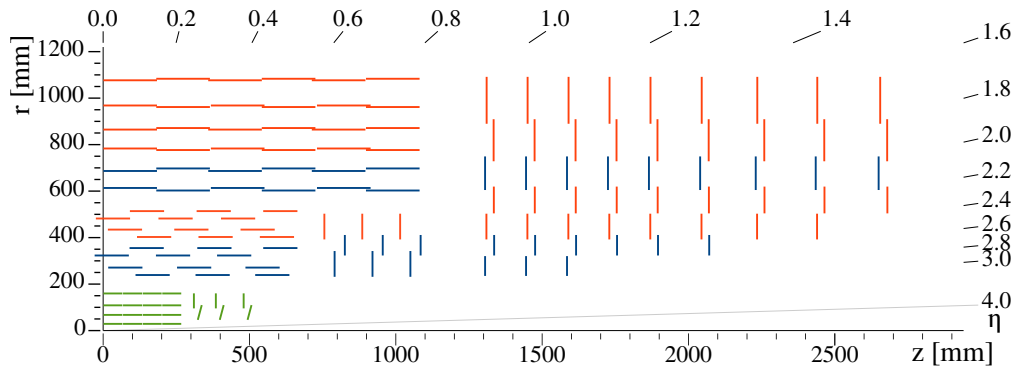


Figure 2.3: An overview of the CMS silicon tracker [29], shown in the  $r$ - $z$  plane after its upgrade during Run-2. The pixel detector is denoted in green while the silicon strip detector is denoted in blue and orange.

Following the pixel detector is the silicon strip detector. It is composed of silicon strips of varying sizes, with increases in size at greater distances to the beam pipe due to the reduced overall particle flux they must contend with. In the barrel region, this consists of 10 layers of silicon strips, while in the endcap regions this consists of nine layers. The latter extend the coverage of the detector to  $|\eta|=2.5$ .

The tracking system provides key information that is essential to the reconstruction of events. As charged particle fly through the CMS detector, their trajectories are curved due to the magnetic field generated by the solenoid magnet (see subsection 2.1.5). By measuring the curvature of these trajectories with this system, the transverse momentum  $p_T$  of particles can be constructed. Additionally, the tracker plays a key role in methods used to determine the nature of hadronic particle cascades and the origin particles (quarks or gluons) from which these originate.

### 2.1.3 The electromagnetic calorimeter

The second innermost subsystem is the electromagnetic calorimeter (ECAL) [31][32]. It is designed to measure the energies of electromagnetic showers initiated by photons and electrons. The ECAL is a homogenous calorimeter, consisting of over 75,000 lead tungstate crystals. These crystals scintillate as charged particles pass through them and the produced photons can be collected via photodiodes, producing an electrical signal. This signal may be evaluated to infer the energy that is deposited. Not only do the crystals scintillate but they are also extremely dense and thus are very effective in absorbing the energy of incoming electrons and photons. This allows a very compact thickness of 23cm (22cm) in the barrel (endcap) region, which corresponds to  $\sim 26$  ( $\sim 25$ ) radiation lengths. An additional component of the ECAL is the preshower detector. This consists of lead absorbers interlaced with scintillating layers and help to distinguish high energy photons from neutral pions. The latter decays into photon pairs which may mimic high energy photons in this part of the detector with an increased likelihood. The increased granularity of the preshower detector helps mitigate this effect. The energy resolution of the ECAL is  $\sim 1\text{-}4\%$ .

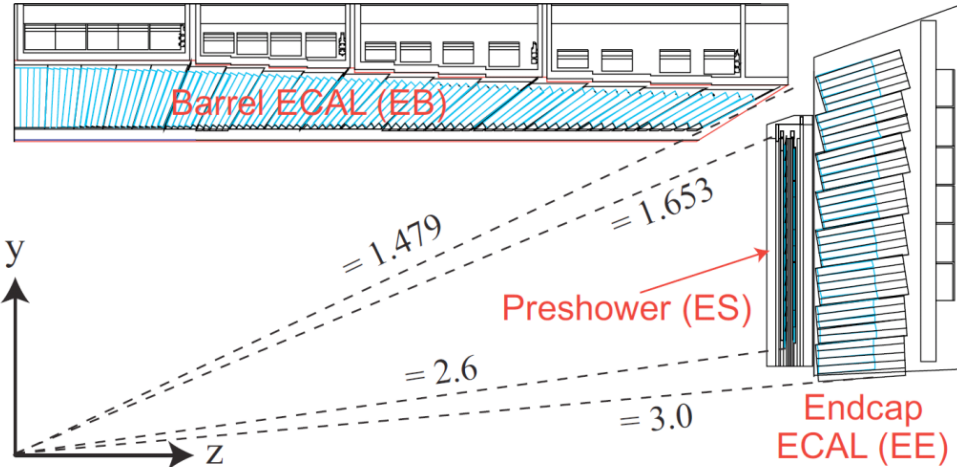


Figure 2.4: An overview of the CMS ECAL [33], shown in the  $r(y)$ - $z$  plane. The dashed lines denote the coverage of the barrel and endcap ECAL region as well as the preshower detector.

#### 2.1.4 The hadronic calorimeter

Following the ECAL is the hadronic calorimeter (HCAL) [34]. It is designed to measure the presence and energy of hadrons, which typically traverse the ECAL with minor energy losses. It is the most hermetic part of the CMS detector, with a coverage out to  $|\eta| = 5.0$ , in order to absorb almost all collision particles. The only exceptions to this are muons which are particles that minimally deposit their energy and neutrinos, which have an interaction probability that is so low that they cannot be measured with the CMS detector at all.

In contrast to the ECAL, the HCAL is a sampling calorimeter. This means layers of absorber are interleaved with layers of a scintillator. Different materials are used in different parts of the calorimeter, which is split into the barrel ( $|\eta| < 1.5$ ), endcap ( $1.5 < |\eta| < 3.0$ ) and forward ( $3.0 < |\eta| < 5.0$ ) regions. Since the HCAL component inside the magnet system does not sufficiently absorb all hadronic showers, the system also extends past the magnet. Due to the sampling nature of the calorimeter, a lower number of respective interaction lengths and larger energy fluctuations in hadronic particle showers, the energy resolution of the HCAL is significantly poorer than the ECAL. It lies in the order of 10-30% and with a strong dependence on the energy and pseudorapidity of the initiating particles.

#### 2.1.5 The superconducting solenoid magnet

A key component of the CMS detector is the superconducting solenoid magnet [35]. It is responsible for maintaining a strong 3.8 T magnetic field that homogeneously permeates the barrel of the detector. A measurement of the field strength can be seen in Figure 2.5. With its toroidal shape, the field is orientated along the  $z$ -axis and covers the 12.9m barrel region of the detector, curving the trajectories of charged particles emerging from the interaction point in the  $\phi$ -direction. This allows for a measurement of the particles transverse momentum  $p_T$ , which together with the  $\phi$  and  $\eta$  directions fully characterise the particle's momentum vector. The magnet itself is composed of superconducting niobium-titanium coils that are cooled to a temperature of

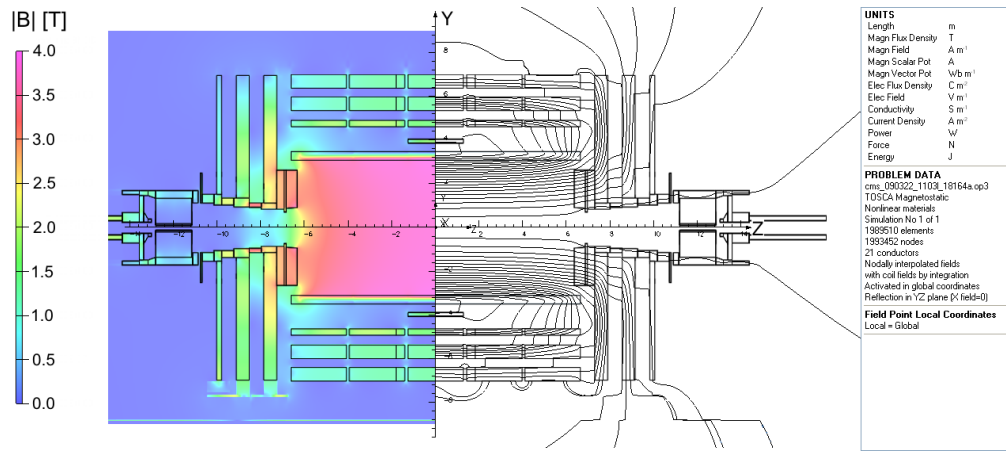


Figure 2.5: An overview of the magnetic flux (left) and magnetic field lines(right) inside the CMS detector, shown in the  $r$ - $z$  plane [36].

4.65K, at which these are superconducting. The magnet is encased by a 12,000t steel yoke that captures the magentic field that is produced outside of the solenoid.

### 2.1.6 The muon chambers

The muon subdetector consists of a dedicated system of gaseous detectors [37][38], which are placed outside of the solenoid magnet. As suggested by the CMS name, a strong focus is placed on the performance of this subdetector. This is as muons may often be produced in collisions that are of physics interest (such as in this work) and thus an emphasis is laid on detecting these with great efficiency. Due to muons being minimally ionising particles, they easily pass through the inner subdetector layers to reach the muon chambers and information from the moun chambers as well as the tracker and calorimeters may be used to identify and reconstruct them.

Like the other subdetectors, the muon chambers are separated in a barrel ( $|\eta| < 1.2$ ) and endcap ( $1.2 < |\eta| < 2.4$ ) region, which are composed of drift tubes and cathode strip chambers respectively. The drift tubes each consists of a gas volume containing a mixture of Argon and CO<sub>2</sub> in which a posititively charged wire is stretched through the center. When charged particles such as muons traverse these tubes, the gas is ionised. Due to the positive charge of the wire, the resulting electrons drift towards the wire producing an electrical signal. Thus the presence of muons may be determined by activation of the drift tubes. The cathode strip chambers on the other hand consist of layers of positively charged (anode) wires, which are arranged in a perpendicular fashion to a set of negatively charged (cathode) strips. Combining signals from both the wires and strips allows for a position measurement in both the  $R$  and  $\phi$  direction. Both types of detector are supplemented by resistive plate chambers, which act as a trigger providing a precise timing resolution of  $\sim$ 1ns. This makes it possible to unambiguously assign muons to individual collisions. These consist of parallel, oppositely charged plastic plates that are coated with a conductive graphite layer and are contained in a gas volume. Ionisation of the gas due to the traversal of a charged particle thus leads to an electrical signal. An overview of the spetial arrangement of these systems can be see in Figure 2.6. With this system, the bulk of muons may be measured with a precise momentum resolution of  $\sim$ 1-2%.

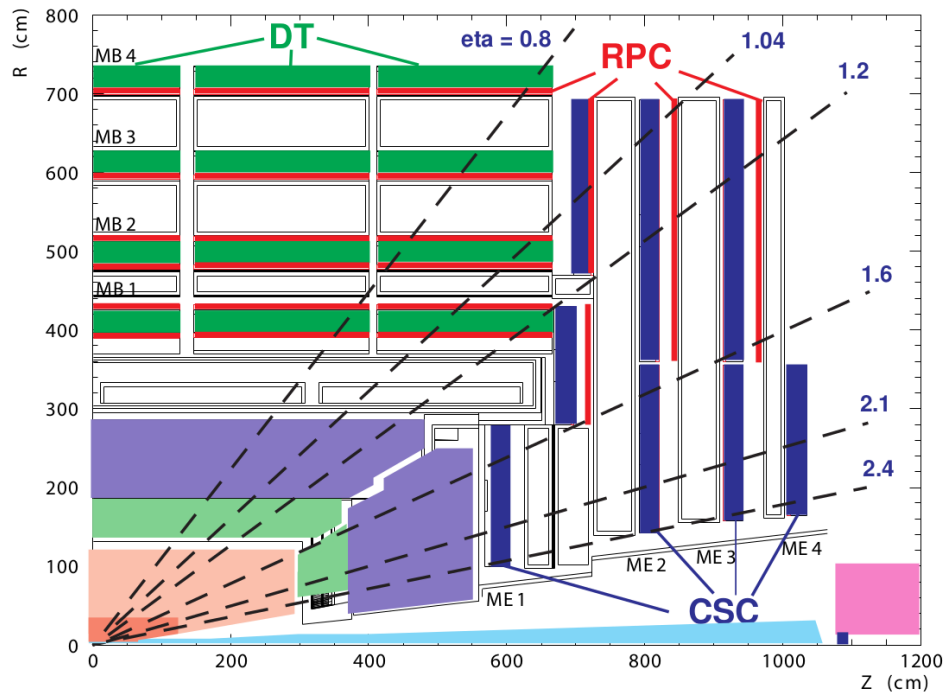


Figure 2.6: An overview of the CMS muon system, shown in the  $r$ - $z$  plane [27]. Shown are the drift tube (DT), the cathode strip chambers (CSC) and resistive plate chambers (RPC).

### 2.1.7 The triggering system

The triggering system is an essential component in managing the data output of the CMS detector [39]. With a nominal collision rate of  $\sim 40$  MHz, the data rate the CMS detector provides is close to 40 TB/s. Not only is the storage of such a quantity of data unfeasible but a significant portion consists of low-energy scattering events which are not of interest. As such, the triggering system is implemented to extract a subset of events that are of physics interest.

The trigger systems is composed of two subsystems. The first the so-called level one (L1) trigger. This is a very fast hardware-based system which reduces the event rate to  $\sim 100$  kHz by evaluating the presence of e.g. energetic muons or other interesting signatures such as large energy deposits in the calorimeters in an event. The total time allocated to decide whether an event should be kept is  $3.2\mu s$ . Subtracting for signal propagation in the detector, the L1 system must make a decision within  $1\mu s$ . From the L1, the events are passed to a software based high-level trigger (HLT) system. This is composed of several thousand CPU cores, performing a simple reconstruction of the event signatures to make a decision whether an event should be stored. Since different analyses have different needs, a set of trigger paths are defined so that only one such path must be satisfied for an event to pass the HLT. Since the HLT is software-based, the trigger paths may be continuously updated. After the HLT, the event rate is thus reduced to  $\sim 100$  Hz and the passing events are permanently stored.

## 2.2 Event reconstruction with the CMS detector

Events that pass the triggering system are stored and reconstructed using a more complicated set of reconstruction algorithms. An overview of the reconstruction techniques for the objects relevant to this work, namely muons and jets, is given in this section.

### 2.2.1 Track and vertex reconstruction

Particle tracks, describing the trajectories of particles through the detector, can be obtained by leveraging information from the pixel and strip detectors of the tracker [40]. By determining the track of a charged particle and thus the curvature of its trajectory in the detectors magnetic field, the particle's transverse momentum  $p_T$  may be implicitly determined. Since track reconstruction is a computationally intensive procedure given the large number of permutations in which individual pixel or strip hits may be combined, this procedure is performed iteratively. Initially, tracks which are easily identifiable due to e.g. their relatively high  $p_T$  or proximity to the interaction point are identified by matching hits in the pixel and silicon strip subdetectors and performing a fitting procedure. The hits associated with these tracks are then removed from the collection of unassociated hits. This procedure is repeated anew with looser fitting criteria so that hits that may originate from low  $p_T$  tracks or those with an origin displaced from the collision point, may also be associated to tracks.

From the reconstructed tracks, common track origins or *vertices* may be identified. Since several proton-proton collisions may occur in a single bunch crossing, this amounts to identifying the location of the individual collisions in an event. Tracks with a low perpendicular distance or low *impact parameter* to the center of the bunch crossing and that satisfy requirements on the number of pixel and strip detector hits as well as the quality of the track fit are chosen for this purpose. These tracks are clustered using a deterministic annealing algorithm [41], thus producing a set of candidate vertices with some location along the z-axis. The vertex candidate

which is associated with the highest  $\sum p_T^2$  is assigned as the primary vertex of the collision. The remaining vertex candidates are referred to as pile-up vertices.

### 2.2.2 The Particle Flow algorithm

The Particle Flow (PF) algorithm [42] is used to combine information from many of the different CMS subsystems to give an improved and holistic description of an event. This includes reconstructed tracks, the energy deposits in the ECAL and HCAL as well as hits in the muon chamber system. Since different types of particles will interact with the CMS subdetector systems in unique ways, the properties of individual particles can be extrapolated from this information. These are briefly summarised in Table 2.1.

Table 2.1: Overview of particle signatures in the CMS detector

Particle	Signature
Muons	Muons produce tracks in the tracker as well as the muon system with minimal energy deposits in the calorimeters.
Electrons	Electrons produce tracks in the tracker as well as energy deposits in the ECAL with minimal deposits in the HCAL.
Photons	Photons do not produce tracks in the tracker due to being uncharged and deposit their energy in the ECAL.
Charged hadrons	Charged hadrons produce tracks in the tracker, primarily depositing their energy in the HCAL.
Neutral hadrons	Neutral hadrons produce no tracks in the tracker, primarily depositing their energy in the HCAL.

A visual overview of these signatures and the particle type they correspond to can be found in Figure 2.7. The PF algorithm leverages exactly these properties. Initially, matched tracks in the tracker and muon systems are identified as muons and the corresponding components are removed from the event. Subsequently, matched tracks and energy deposit clusters in the ECAL are identified as electrons and the corresponding components are removed. An isolated cluster in the ECAL with no associated track is reconstructed as a photon candidate and the corresponding cluster is removed. This is expected to leave only charged and neutral hadrons. Clusters of energy deposits in the HCAL associated with a track are thus identified as charged hadrons. However, it frequently occurs that photons are produced in the decay of neutral hadrons. Thus, if the energy estimated from a track is considerably less than the associated cluster in the HCAL and there is a corresponding energy deposit in the ECAL, an additional photon candidate is reconstructed that is associated with the hadron. Finally, HCAL clusters with no associated track are reconstructed as neutral hadrons.

This of course is a greatly simplified description, a more comprehensive version of which can be found in [42]. The following section describe in greater detail the reconstruction of objects relevant to this work. This includes muons, *jets*, which are collimated particle showers that typically consist of a collection of reconstructed objects and missing transverse energy.

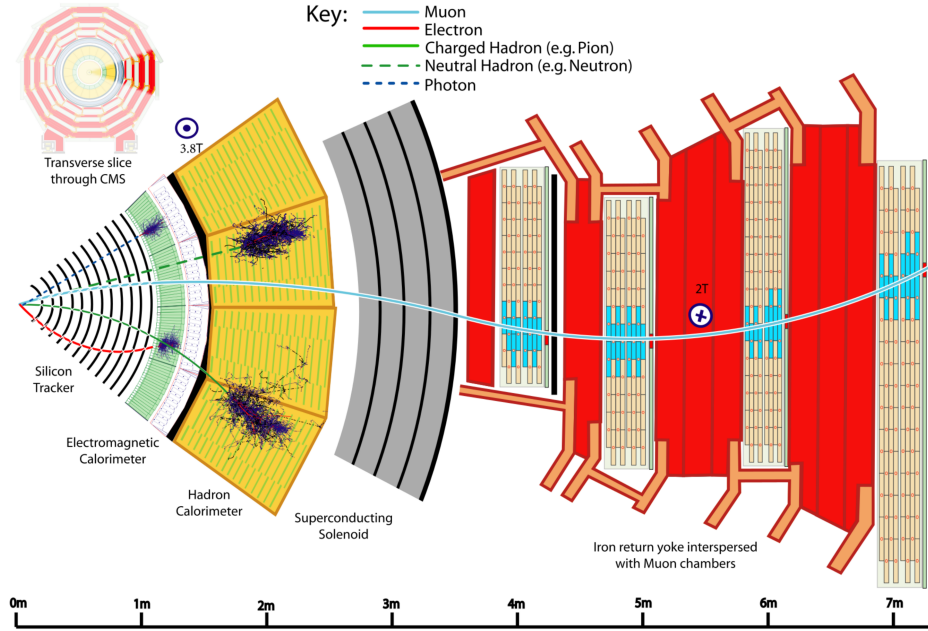


Figure 2.7: A transverse slice of the CMS detector, visualising the signatures that different particles produce in the different detector subsystems. [42].

### 2.2.3 Reconstruction and identification of muons

Since muons are used to reconstruct the Higgs candidate in the cH, they represent an important element of the analysis described in this work. Using the available information from the tracker and muon system, three different approaches may be used to initially reconstruct muon tracks.

- **Standalone muon tracks:** A standalone muon track simply refers by a fit of individual hits present in the muon detector.
- **Tracker muon tracks:** Tracker muon tracks are reconstructed by extrapolating tracks from the tracker to the muon detector, referred to as an *inside-out* approach. If a hit in the muon detector can be matched to the extrapolated track, then these matched tracks are identified as a tracker muon track. This reduces the impact from atmospheric muons traversing the detector, which may be falsely interpreted as standalone muon tracks.
- **Global muon tracks:** Global muon tracks are obtained through an *outside-in* approach, by matching standalone muon tracks with tracker muon tracks through a comparison of the respective fitted track parameters. If the tracks are found to match, a combined fit of these tracks is performed. This approach reduces the impact from remnants of hadronic showers that reach the muon chambers, which may be incorrectly reconstructed as a tracker muon track.

Naturally, there is a large overlap between global and tracker muon tracks. If two muon tracks share the same track in the tracker, then they are merged into a single object. The collection of standalone, tracker and global muons is passed to the previously introduced PF algorithm

which, by imposing additional quality requirements (see [42]) produces a set of reconstructed muon candidates.

A useful criterium in identifying muons that originate directly from the proton-proton interaction is the relative isolation  $\mathcal{I}^2$ . This is defined as

$$\mathcal{I}_{\text{rel}}^\mu = \left( \sum p_T^{\text{charged}} + \max \left( \sum p_T^{\text{neutral}} + \sum p_{T\gamma} - p_T^{\mu,\text{PU}} \right) \right) / p_T^\mu. \quad (2.4)$$

Here,  $\sum p_T^{\text{charged}}$  represents the scalar sum of the transverse momenta of charged hadron originating from the primary vertex of the event. The quantities  $\sum p_T^{\text{neutral}}$  and  $\sum p_{T\gamma}$  represent the respective transverse momenta sums for neutral hadrons and photons. These sums are calculated by accounting from contributions within a conical volume around the muon direction. The size of a cone between two positions  $i$  and  $j$  is defined as  $\Delta R(i, j) = \sqrt{\Delta\eta(i, j)^2 + \Delta\phi(i, j)^2}$  and in this case the cone boundary around the muon direction is set at  $\Delta R = 0.4$ . The contribution to the relative isolation from pile-up is estimated by subtracting  $p_T^{\mu,\text{PU}} = 0.5 \sum_k p_T^{k,\text{charged}}$  in Equation 2.4, where the sum over  $k$  represents charged hadron contributions not originating from the PV. The factor 0.5 corrects for different fractions of charged and neutral particles in the cone [43]. Lastly,  $p_T^\mu$  represents the transverse momentum of the muon. The relative isolation is thus a variable that quantifies the presence of energy deposits in the ECAL and HCAL around the trajectory of the muon. Since muons are expected to produce such deposits only minimally, good muon candidates are expected to be associated with small values of  $\mathcal{I}_{\text{rel}}^\mu$ .

Two sets of muon identification criteria are defined for this work:

- **Loose muons:** Loose muons are PF muons reconstructed from either a global or tracker muon track where the perpendicular distance of the extrapolated track to the event's primary vertex is less than 5mm in the  $z$  direction and less than 2mm in the  $r$  direction.
- **Tight muons:** Tight muons are loose muons which are reconstructed exclusively from a global muon track. A number of additional criteria are applied. This includes that the fit quality of the global muon track must be  $\chi^2/\text{ndf} < 10$  as well that the significance of the track's 3D impact parameter  $\text{SIP}_{3\text{D}} = \text{IP}/\sigma_{\text{IP}}$  satisfies  $\text{SIP}_{3\text{D}} < 4$ . Here IP is the impact parameter or point of closest approach to the primary vertex and  $\sigma_{\text{IP}}$  is the associated uncertainty. Additionally, it is required the at least six layers with at least one pixel hits are registered in the tracker in the associated track as well as two segments hit in the muon detector. Lastly, a relative isolation requirement of  $\mathcal{I}_{\text{rel}}^\mu < 0.25$  is imposed.

The tight muon definition is used to select muons for reconstructing Higgs candidates while the loose definition is used in the estimation of reducible backgrounds.

#### 2.2.4 Reconstruction and identification of jets

The quarks and gluons that are produced in pp collisions rapidly hadronise, typically producing collimated cones of particle referred to as *jets*. Details on the concept of hadronisation, which results from the nature of the strong interaction, can be found in [44]. Since the c quark of the cH process too will produce a jet, jet objects also represent an important aspect of the analysis presented in this work.

To produce jet objects, the hadrons reconstructed by the PF algorithm must be clustered. To

ensure a minimal impact of pile-up on this clustering, the contributions of pile-up are mitigated through *charged hadron subtraction*. This invokes the removal of charged hadron contributions in the HCAL and ECAL if these may be associated with any of the pile-up vertices produced in the collision, as described in subsection 2.2.1. Once this subtraction has been performed, the remaining PF hadrons are passed to the anti- $k_T$  algorithm [45]. The anti- $k_T$  algorithm is an iterative clustering algorithm that is based on a principle of minimal distances between particles. The distance  $d_{ij}$  between the particles  $i$  and  $j$  is defined as well as the distance  $d_{iB}$  between particle  $i$  and the beam. These are given by

$$d_{ij} = \min\left(\frac{1}{p_{T,i}}, \frac{1}{p_{T,j}}\right) \frac{\Delta_{ij}^2}{R^2} \quad (2.5)$$

$$d_{iB} = \frac{1}{p_{T,i}} \quad (2.6)$$

$$\Delta_{ij} = \sqrt{\Delta y(i,j)^2 + \Delta\phi(i,j)^2}. \quad (2.7)$$

Here,  $y$  is the rapidity of a particle and  $R$  is a constant parameter that determines the cone size of the clustered jets. The default choice used in CMS is  $R=0.4$ , which is also used in this work. Starting with the highest  $p_T$  object in the initial iteration, the distance  $d_{ij}$  with the closest PF candidate  $j$  is calculated. The two objects are clustered together and this process is repeated until a stopping condition  $d_{ih} > d_{iB}$  is met. At this point, the jet is considered fully reconstructed and the PF candidates used in its clustering are removed for the reconstruction of subsequent jets.

Due to the presence of detector noise, unphysical low  $p_T$  jets can be erroneously reconstructed. This effect can be mitigated by applying additional criteria on reconstructed jets. This includes requiring that at least two PF candidates are clustered in the jet and that the jet's energy is not solely attributed to neutral hadrons or photons. These requirements remove almost all such unphysical jets while over 99% of physical jets fulfill them [46]. Additionally, a pile-up discrimination algorithm is described in [46], of which the loose working point is applied to jets with  $p_T < 50$  GeV in this work.

A calibration of jet energies is performed after reconstruction [47] in both simulation and data. This calibration accounts for pile-up contributions in the clustering, the non-linearity of the detector response and improper reconstruction of hadrons. A number of methods are used to derive sets of correction factors. An example is the use of events with a Z boson, the  $p_T$  of which may be precisely reconstructed via the  $Z \rightarrow \mu\mu$  decay, that a single jet recoils against. Additionally, significant discrepancies in the resolution of jets in simulation and data are observed, with the resolution being worse in the latter than the former. This is accounted for by a smearing method, in which the resolution of jets is artificially smeared in simulation so that a better comparison to data is achieved.

### 2.2.5 Missing transverse momentum

Due to the conservation of momentum, it is expected that the vectorial sum of momenta of all particles produced in a collision adds up to zero. However, this may not be the case when particles such as neutrinos are produced in a collision as these cannot be measured by the detector. As a

result, it can be useful to define the missing transverse momentum as

$$p_T^{\text{miss}} = \sum_i^{\text{PF}} p_T^{(i)}. \quad (2.8)$$

The presence of significant quantities of  $p_T^{\text{miss}}$  may thus be used to identify the presence of neutrinos in an event.

## 2.3 Identification of charm quark-induced jets

To identify the charm quark-induced jet of the cH process, one must be able to discriminate against both bottom quark as well as light quark or gluon-induced jets. This is a task often colloquially referred to as *flavour tagging*, with a jet's *flavour* being determined by the type of particle that initiated it. Modern flavour tagging techniques typically use machine learning to leverage key jet properties that may differentiate jets of different flavours, though this remains a challenging task. To discuss these properties, a definition of jet flavour is useful. In the context of CMS, a ghost matching procedure [48] is applied to obtain such a definition for simulated events. This involves adding information from the event simulation to the reconstructed event. Specifically, hadrons containing bottom and charm quarks are identified in the simulation and added to the list of reconstructed PF candidates, albeit with negligible momenta. With this addition of so-called *ghost hadrons* the jet clustering is once again performed. Due to the negligible momenta of the ghost hadrons, the clustering procedure itself is unaffected. However, the inclusion of the ghost hadrons can be used for the following definitions:

- ***c* jets:** If at least one charm (*c*) ghost hadron and no bottom (*b*) hadrons are clustered inside the jet, the jet is labelled as a *c* jet.
- ***b* jets:** If at least one *b* ghost hadron is clustered inside the jet, the jet is labelled as a *b* jet.
- **light jets:** If no ghost hadrons are clustered inside the jet, the jet is labelled as a light jet. Light jets may be initiated by quarks such as the up, down, or strange quark or by gluons. An additional, technical category of *pile-up jets* exists depending on whether so-called matching criteria between reconstructed and simulated jets are fulfilled, though they are subsumed into the light jets category for the purpose of this work.

The task of identifying *c* jets is thus twofold, as *c* jets must be differentiated from both *b* jets and light (pileup) jets. This is broken down into two tasks:

1. Discriminating *heavy-flavour* (HF) jets consisting of *b* jets and *c* jets against light jets.
2. Discriminating between *b* jets and *c* jets.

### 2.3.1 Properties of heavy-flavour jets

The term heavy-flavour originates from the mass of the bottom and charm quarks, which is an order of magnitude greater than the next heaviest quark, the strange quark. Similarly, *c* and *b* hadrons have relatively long lifetimes that allow them to travel an observable distance from the PV before decaying. The typical lifetime of a *b* hadron of the order of  $\sim 1.5$  ps while that of *c* quarks ranges down to approximately an order of magnitude less [1]. This typically results in

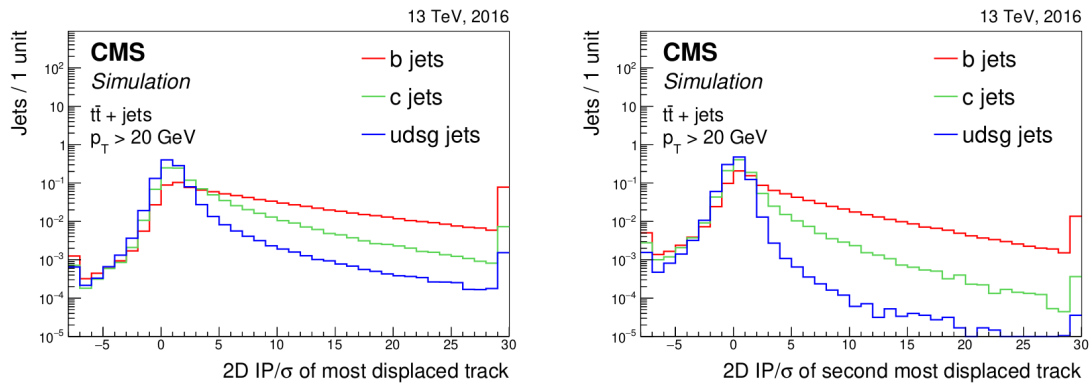


Figure 2.8: Plots showing the significance of the 2D impact parameter of the most and second most displaced tracks in a jet [49]. As can be seen, these variables can differentiate  $b$  and  $c$  jets from light jets to a significant degree.

the presence of a secondary vertex (SV) that is measurably displaced from the collision point up to a distance of 1cm in the case of energetic hadrons and is thus a key signature of HF jets. Tracks originating from the decay of a HF induced jet thus typically originate from a SV. This effect can for example be seen when looking at the significance of 2D impact parameters of  $b$ ,  $c$  and light jets, as seen in Figure 2.8.

Another feature of heavy flavour jets is the presence of leptons in the jet. This results from the relatively large branching fractions of HF hadrons into states containing leptons. These are typically low-energy and are present in about 20% (10%) of  $b(c)$  jets, meaning the identification of a low-energy electron or muon inside a jet serves as a good indicator that a jet originates from a HF hadron. Also of significance are the relatively high masses HF hadrons exhibit in comparison to their lighter counterparts. This results in HF induced jets having a broader energy flux compared to their lighter counterparts, due to higher diffusion of momenta perpendicular to the flight direction as well as a higher hadron multiplicity resulting from the decay of the HF hadron. These features are illustrated in Figure 2.9.

### 2.3.2 The DeepJet algorithm

The *DeepJet* algorithm [50] is a machine learning algorithm used for jet-flavour identification in this work. It improves on previous neural network based algorithms [49] used by CMS in the Run-2 period of the LHC. A notable feature compared to earlier algorithms is its use of lower level information such as use of track, PV and SV information, as well as PF candidate and event kinematics information. An overview of the architecture employed by DeepJet can be seen in Figure 2.10. The network is comprised of three branches that individually process neutral and charged hadrons as well as secondary vertices before this information is combined with global variables in a set of fully connected layers. The network output consists of six output nodes representing six individual output classes. The output value of the nodes  $\mathcal{P}(b/bb/lepb/c/l/g)$  for a given jet are interpreted as the likelihood that a jet belongs to the respective class. These are defined as

- **$b/bb/lepb$  ( $b$  jets):** These three classes represent subclasses of jets originating from a  $b$  hadron. The  $b$  class represents a jet originating from a single  $b$  hadron, the  $bb$  class

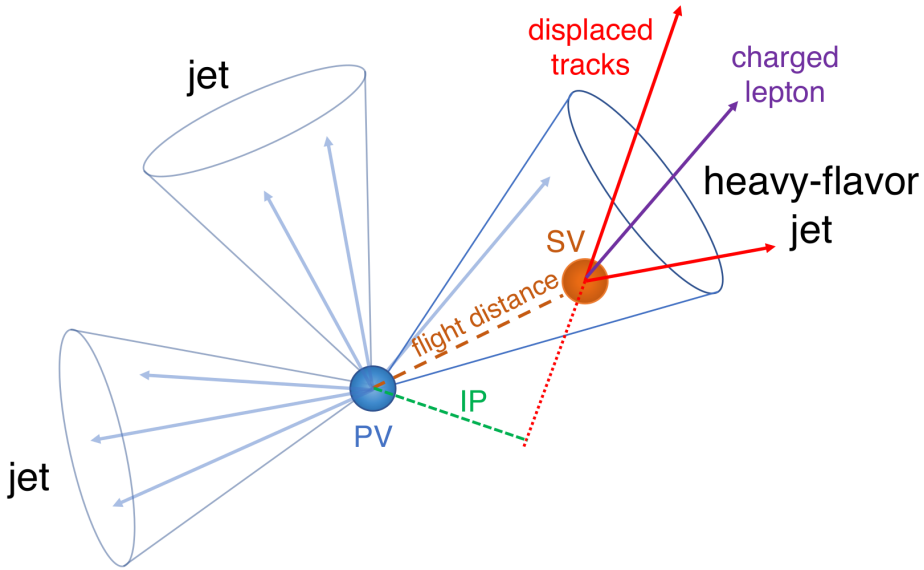


Figure 2.9: An illustration highlighting the properties of HF jets [49]. The presence of a secondary vertex (SV), characterised by the impact parameter (IP) in green, as well as the presence of a lepton is highlighted.

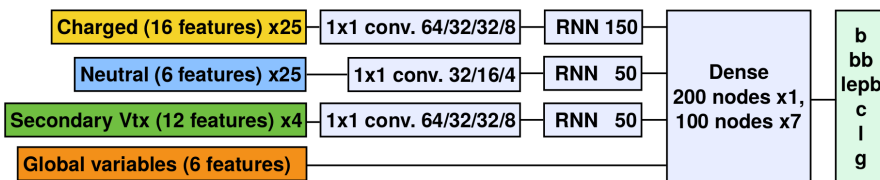


Figure 2.10: An illustration depicting the architecture of the DeepJet neural network [50]. Three individual branches separately process the charged hadrons, neutral hadrons and secondary vertex information before being passed onto a combining, fully connected layer together with global variables.

originating from two  $b$  hadrons and  $lepb$  representing a jet originating from a  $b$  hadron with the presence of a soft lepton.

- **$c$  ( $c$  jets):** This class represents a jet originating from a  $c$  hadron.
- **$l, g$  (light jets):** These two classes represent light jets originating from a light quark or gluon respectively.

From these output classes, two useful discriminators to identify  $c$  jets can be constructed. These are

$$CvsL = \frac{\mathcal{P}(c)}{\mathcal{P}(c) + \mathcal{P}(l) + \mathcal{P}(g)} \quad (2.9)$$

$$CvsB = \frac{\mathcal{P}(c)}{\mathcal{P}(c) + \mathcal{P}(b) + \mathcal{P}(bb) + \mathcal{P}(lepb)}, \quad (2.10)$$

representing a discrimination of  $c$  jets against  $b$  jets and light jets respectively. The performance of DeepJet with the  $CvsL$  and  $CvsB$  discriminators in simulated samples of top quark pair production can be seen in Figure 2.11. A comparison to the *DeepCSV* jet-flavour identification algorithm is included, highlighting the performance gain that the DeepJet algorithm achieves.

Since neural network based algorithms are trained on simulated samples that do not perfectly describe their data counterpart, the neural network output must be calibrated with respect to data. To calibrate the entire shape of the algorithm's output distributions the approach described in [51] is used. This involves targeting phase spaces enriched in  $b$  jets (top quark pair production),  $c$  jets (charm associated  $W^\pm$  production) and light jets (jet associated Drell-Yan production). Using simulation, the fractions of  $b$ ,  $c$  and light-flavour jets are determined in each phase space and an iterative fitting procedure, minimising differences between simulation and data is performed. This allows for the derivation of correction factors which depend on the discriminators  $CvsL$  and  $CvsB$  as well as the true flavour of a simulated jet.

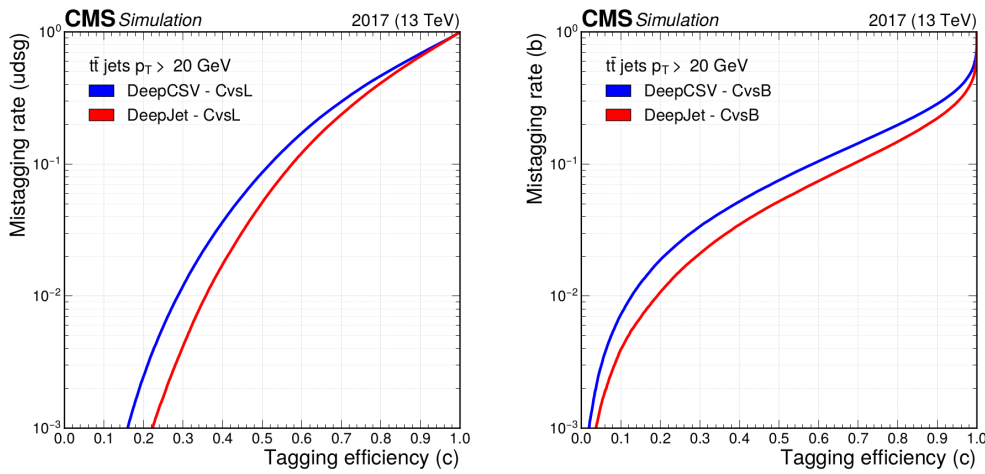


Figure 2.11: Performance of DeepJet algorithm in identifying  $c$  jets against  $b$  jets and light jets in simulated samples of top quark pair production, in which both top quarks decay hadronically [51]. The x-axis represents the efficiency with which  $c$  jets are identified, while the y-axis represents mis-identification rate with respect to either  $b$  jets or light jets.



## Chapter 3

# Search for the cH( $ZZ \rightarrow 4\mu$ ) process



## Chapter 4

# An EFT interpretation of the $cH(ZZ \rightarrow 4\mu)$ process



# Conclusion



# Bibliography

- [1] S. Navas et al. “Review of Particle Physics”. In: *Phys. Rev. D* 110 (3 Aug. 2024), p. 030001. DOI: 10.1103/PhysRevD.110.030001. URL: <https://link.aps.org/doi/10.1103/PhysRevD.110.030001>.
- [2] P.W. Higgs. “Broken Symmetries and the Masses of Gauge Bosons”. In: *Phys. Rev. Lett.* 13 (16 Oct. 1964), pp. 508–509. DOI: 10.1103/PhysRevLett.13.508. URL: <https://link.aps.org/doi/10.1103/PhysRevLett.13.508>.
- [3] F. Englert and R. Brout. “Broken Symmetry and the Mass of Gauge Vector Mesons”. In: *Phys. Rev. Lett.* 13 (9 Aug. 1964), pp. 321–323. DOI: 10.1103/PhysRevLett.13.321. URL: <https://link.aps.org/doi/10.1103/PhysRevLett.13.321>.
- [4] CMS Collaboration. “Observation of a new boson at a mass of 125 GeV with the CMS experiment at the LHC”. In: *Physics Letters B* 716 (1 2012), pp. 30–61. DOI: 10.1016/j.physletb.2012.08.021.. URL: <https://www.sciencedirect.com/science/article/pii/S0370269312008581>.
- [5] G. Aad et al. “Observation of a new particle in the search for the Standard Model Higgs boson with the ATLAS detector at the LHC”. In: *Physics Letters B* 716.1 (2012), pp. 1–29. ISSN: 0370-2693. DOI: 10.1016/j.physletb.2012.08.020. URL: <https://www.sciencedirect.com/science/article/pii/S037026931200857X>.
- [6] CMS Collaboration. “A portrait of the Higgs boson by the CMS experiment ten years after the discovery”. en. In: *Nature* 607.7917 (July 2022), pp. 60–68. DOI: 10.1038/s41586-022-04892-x. URL: <http://dx.doi.org/10.1038/s41586-022-04892-x>.
- [7] Nina M. Coyle, Carlos E. M. Wagner, and Viska Wei. “Bounding the charm Yukawa coupling”. In: *Phys. Rev. D* 100 (7 Oct. 2019), p. 073013. DOI: 10.1103/PhysRevD.100.073013. URL: <https://link.aps.org/doi/10.1103/PhysRevD.100.073013>.
- [8] Michael Edward Peskin and Daniel V. Schroeder. *An Introduction to Quantum Field Theory*. Reading, USA: Addison-Wesley (1995) 842 p. Westview Press, 1995.
- [9] R. Wolf. *The Higgs Boson Discovery at the Large Hadron Collider*. Springer, 2015. ISBN: 978-3-319-18512-5, 978-3-319-18511-8. DOI: 10.1007/978-3-319-18512-5.
- [10] G. Arnison et al. “Experimental observation of isolated large transverse energy electrons with associated missing energy at s=540 GeV”. In: *Physics Letters B* 122.1 (1983), pp. 103–116. ISSN: 0370-2693. DOI: 10.1016/0370-2693(83)91177-2. URL: <https://www.sciencedirect.com/science/article/pii/0370269383911772>.
- [11] J. Goldstone, A. Salam, and S. Weinberg. “Broken Symmetries”. In: *Phys. Rev.* 127 (3 Aug. 1962), pp. 965–970. DOI: 10.1103/PhysRev.127.965. URL: <https://link.aps.org/doi/10.1103/PhysRev.127.965>.

- [12] CMS Collaboration. *Simultaneous probe of the charm and bottom quark Yukawa couplings using ttH events*. 2025. DOI: 10.48550/arXiv.2509.22535. arXiv: 2509.22535 [hep-ex]. URL: <https://arxiv.org/abs/2509.22535>.
- [13] CMS Collaboration. *Search for a Higgs boson produced in association with a charm quark and decaying to a W boson pair in proton-proton collisions at  $\sqrt{s} = 13$  TeV*. 2025. arXiv: 2508.14988 [hep-ex]. URL: <https://arxiv.org/abs/2508.14988>.
- [14] CMS Collaboration. *Search for the associated production of a Higgs boson with a charm quark in the diphoton decay channel in pp collisions at  $\sqrt{s} = 13$  TeV*. 2025. arXiv: 2503.08797 [hep-ex]. URL: <https://arxiv.org/abs/2503.08797>.
- [15] Nuoyu Dong et al. “Probing charm Yukawa coupling through ch associated production at the hadron colliders”. In: *Phys. Rev. D* 111 (5 Mar. 2025), p. 053003. DOI: 10.1103/PhysRevD.111.053003. URL: <https://link.aps.org/doi/10.1103/PhysRevD.111.053003>.
- [16] C T Potter et al. *Handbook of LHC Higgs Cross Sections: 3. Higgs Properties: Report of the LHC Higgs Cross Section Working Group*. en. 2013. DOI: 10.5170/CERN-2013-004. URL: <http://cds.cern.ch/record/1559921>.
- [17] J. A. Aguilar-Saavedra, J. M. Cano, and J. M. No. “More light on Higgs flavor at the LHC: Higgs boson couplings to light quarks through  $h + \gamma$  production”. In: *Phys. Rev. D* 103 (9 May 2021), p. 095023. DOI: 10.1103/PhysRevD.103.095023. URL: <https://link.aps.org/doi/10.1103/PhysRevD.103.095023>.
- [18] The CMS Collaboration. “Combined measurements of Higgs boson couplings in proton-proton collisions at  $\sqrt{s} = 13$  TeV”. In: *The European Physical Journal C* 79.5 (May 2019). ISSN: 1434-6052. DOI: 10.1140/epjc/s10052-019-6909-y. URL: <http://dx.doi.org/10.1140/epjc/s10052-019-6909-y>.
- [19] Steven Weinberg. “Baryon and Lepton Nonconserving Processes”. In: *Phys. Rev. Lett.* 43 (1979), pp. 1566–1570. DOI: 10.1103/PhysRevLett.43.1566.
- [20] B. Grzadkowski et al. “Dimension-six terms in the Standard Model Lagrangian”. In: *Journal of High Energy Physics* 2010.10 (Oct. 2010). ISSN: 1029-8479. DOI: 10.1007/jhep10(2010)085. URL: [http://dx.doi.org/10.1007/JHEP10\(2010\)085](http://dx.doi.org/10.1007/JHEP10(2010)085).
- [21] Gino Isidori, Felix Wilsch, and Daniel Wyler. “The standard model effective field theory at work”. In: *Reviews of Modern Physics* 96.1 (Mar. 2024). ISSN: 1539-0756. DOI: 10.1103/revmodphys.96.015006. URL: <http://dx.doi.org/10.1103/RevModPhys.96.015006>.
- [22] Joseph Bramante et al. “Boosted Higgs bosons from chromomagnetic b’s:  $b\bar{b}h$  at high luminosity”. In: *Phys. Rev. D* 93 (5 Mar. 2016), p. 053001. DOI: 10.1103/PhysRevD.93.053001. URL: <https://link.aps.org/doi/10.1103/PhysRevD.93.053001>.
- [23] J. Elias-Miró et al. “Higgs windows to new physics through d=6 operators: constraints and one-loop anomalous dimensions”. In: *Journal of High Energy Physics* 2013.11 (Nov. 2013). ISSN: 1029-8479. DOI: 10.1007/jhep11(2013)066. URL: [http://dx.doi.org/10.1007/JHEP11\(2013\)066](http://dx.doi.org/10.1007/JHEP11(2013)066).
- [24] The CMS Collaboration. “The CMS experiment at the CERN LHC”. In: *Journal of Instrumentation* 3.08 (Aug. 2008), S08004. DOI: 10.1088/1748-0221/3/08/S08004. URL: <https://doi.org/10.1088/1748-0221/3/08/S08004>.
- [25] Oliver Sim Brüning et al. *LHC Design Report*. CERN Yellow Reports: Monographs. Geneva: CERN, 2004. DOI: 10.5170/CERN-2004-003-V-1. URL: <http://cds.cern.ch/record/782076>.

- [26] E. A. Mobs. “The CERN accelerator complex. Complex des accélérateurs du CERN”. In: (Oct. 2016). General Photo. URL: <http://cds.cern.ch/record/2225847>.
- [27] The CMS Collaboration. *CMS Physics : Technical Design Report Volume 1: Detector Performance and Software*. Technical design report. CMS. Geneva: CERN, 2006. URL: <https://cds.cern.ch/record/922757>.
- [28] CMS Collaboration. “Development of the CMS detector for the CERN LHC Run 3”. In: *Journal of Instrumentation* 19.05 (May 2024), P05064. ISSN: 1748-0221. DOI: 10.1088/1748-0221/19/05/p05064. URL: <http://dx.doi.org/10.1088/1748-0221/19/05/P05064>.
- [29] *CMS Tracker Detector Performance Public Results*. Last accessed 24.11.25. URL: <https://twiki.cern.ch/twiki/bin/view/CMSPublic/DPGResultsTRK>.
- [30] The CMS Collaboration. “Description and performance of track and primary-vertex reconstruction with the CMS tracker”. In: *Journal of Instrumentation* 9.10 (Oct. 2014), P10009–P10009. ISSN: 1748-0221. DOI: 10.1088/1748-0221/9/10/p10009. URL: <http://dx.doi.org/10.1088/1748-0221/9/10/P10009>.
- [31] CMS Collaboration. *The CMS electromagnetic calorimeter project: Technical Design Report*. Tech. rep. Geneva, 1997. URL: <https://cds.cern.ch/record/349375>.
- [32] CMS Collaboration. *The CMS ECAL performance with examples*. Tech. rep. Geneva: CERN, 2014. DOI: 10.1088/1748-0221/9/02/C02008. URL: <https://cds.cern.ch/record/1632384>.
- [33] CMS Collaboration. *The CMS ECAL performance with examples*. Tech. rep. Geneva: CERN, 2014. DOI: 10.1088/1748-0221/9/02/C02008. URL: <https://cds.cern.ch/record/1632384>.
- [34] CMS Collaboration. *The CMS hadron calorimeter project: Technical Design Report*. Tech. rep. Geneva, 1997. URL: <https://cds.cern.ch/record/357153>.
- [35] CMS Collaboration. *The CMS magnet project: Technical Design Report*. Tech. rep. Geneva, 1997. URL: <https://cds.cern.ch/record/331056>.
- [36] CMS Collaboration. “Precise mapping of the magnetic field in the CMS barrel yoke using cosmic rays”. In: *Journal of Instrumentation* 5.03 (Mar. 2010), T03021–T03021. ISSN: 1748-0221. DOI: 10.1088/1748-0221/5/03/t03021. URL: <http://dx.doi.org/10.1088/1748-0221/5/03/T03021>.
- [37] CMS Collaboration. *The CMS muon project: Technical Design Report*. Tech. rep. Geneva, 1997. URL: <https://cds.cern.ch/record/343814>.
- [38] The CMS collaboration. “Performance of CMS muon reconstruction in pp collision events at  $\sqrt{s} = 7\text{TeV}$ ”. In: *Journal of Instrumentation* 7.10 (Oct. 2012), P10002–P10002. ISSN: 1748-0221. DOI: 10.1088/1748-0221/7/10/p10002. URL: <http://dx.doi.org/10.1088/1748-0221/7/10/P10002>.
- [39] Mia Tosi. *The CMS trigger in Run 2*. Tech. rep. Geneva: CERN, Oct. 2017. DOI: 10.22323/1.314.0523. URL: <https://cds.cern.ch/record/2290106>.
- [40] CMS collaboration et al. “Description and performance of track and primary-vertex reconstruction with the CMS tracker”. In: *Journal of Instrumentation* 9.10 (2014), P10009.
- [41] K. Rose. “Deterministic annealing for clustering, compression, classification, regression, and related optimization problems”. In: *Proceedings of the IEEE* 86.11 (1998), pp. 2210–2239. DOI: 10.1109/5.726788.

- [42] A. M. Sirunyan et al. “Particle-flow reconstruction and global event description with the CMS detector.” In: *JINST* 12 (June 2017). Replaced with the published version. Added the journal reference and DOI. All the figures and tables can be found at <http://cms-results.web.cern.ch/cms-results/public-results/publications/PRF-14-001>(CMS Public Pages), P10003. 82 p. DOI: 10.1088/1748-0221/12/10/P10003. arXiv: 1706.04965. URL: <https://cds.cern.ch/record/2270046>.
- [43] CMS Collaboration. “Pileup mitigation at CMS in 13 TeV data”. In: *Journal of Instrumentation* 15.09 (Sept. 2020), P09018–P09018. ISSN: 1748-0221. DOI: 10.1088/1748-0221/15/09/p09018. URL: <http://dx.doi.org/10.1088/1748-0221/15/09/P09018>.
- [44] B. Andersson et al. “Parton fragmentation and string dynamics”. In: *Physics Reports* 97.2 (1983), pp. 31–145. ISSN: 0370-1573. DOI: [https://doi.org/10.1016/0370-1573\(83\)90080-7](https://doi.org/10.1016/0370-1573(83)90080-7). URL: <https://www.sciencedirect.com/science/article/pii/0370157383900807>.
- [45] M. Cacciari et al. “FastJet user manual”. In: *The European Physical Journal C* 72.3 (Mar. 2012), p. 1896. ISSN: 1434-6052. DOI: 10.1140/epjc/s10052-012-1896-2. URL: <https://doi.org/10.1140/epjc/s10052-012-1896-2>.
- [46] CMS Collaboration. *Jet algorithms performance in 13 TeV data*. Tech. rep. Geneva: CERN, 2017. URL: <https://cds.cern.ch/record/2256875>.
- [47] CMS Collaboration. “Jet energy scale and resolution in the CMS experiment in pp collisions at 8 TeV”. In: *Journal of Instrumentation* 12.02 (Feb. 2017), P02014–P02014. ISSN: 1748-0221. DOI: 10.1088/1748-0221/12/02/p02014. URL: <http://dx.doi.org/10.1088/1748-0221/12/02/P02014>.
- [48] Matteo Cacciari and Gavin P. Salam. “Pileup subtraction using jet areas”. In: *Physics Letters B* 659.1–2 (Jan. 2008), pp. 119–126. ISSN: 0370-2693. DOI: 10.1016/j.physletb.2007.09.077. URL: <http://dx.doi.org/10.1016/j.physletb.2007.09.077>.
- [49] CMS Collaboration. “Identification of heavy-flavour jets with the CMS detector in pp collisions at 13 TeV”. In: *Journal of Instrumentation* 13.05 (May 2018), P05011–P05011. ISSN: 1748-0221. DOI: 10.1088/1748-0221/13/05/p05011. URL: <http://dx.doi.org/10.1088/1748-0221/13/05/P05011>.
- [50] E. Bols et al. “Jet flavour classification using DeepJet”. In: *Journal of Instrumentation* 15.12 (Dec. 2020), P12012–P12012. ISSN: 1748-0221. DOI: 10.1088/1748-0221/15/12/p12012. URL: <http://dx.doi.org/10.1088/1748-0221/15/12/P12012>.
- [51] CMS Collaboration. “A new calibration method for charm jet identification validated with proton-proton collision events at  $\sqrt{s} = 13$  TeV”. In: *Journal of Instrumentation* 17.03 (Mar. 2022), P03014. ISSN: 1748-0221. DOI: 10.1088/1748-0221/17/03/p03014. URL: <http://dx.doi.org/10.1088/1748-0221/17/03/P03014>.